

Spatially Explicit Spectral Analysis of Point Clouds and Geospatial Data.

Daniel Buscombe*

Grand Canyon Monitoring and Research Center, Southwest Biological Science Center, U.S. Geological Survey, Flagstaff, Arizona, USA

Abstract

The increasing use of spatially explicit analyses of high-resolution spatially distributed data (imagery and point clouds) for the purposes of characterising spatial heterogeneity in geophysical phenomena necessitates the development of custom analytical and computational tools. In recent years, such analyses have become the basis of, for example, automated texture characterisation and segmentation, roughness and grain size calculation, and feature detection and classification, from a variety of data types. In this work, much use has been made of statistical descriptors of localised spatial variations in amplitude variance (roughness), however the horizontal scale (wavelength) and spacing of roughness elements is rarely considered. This is despite the fact that the ratio of characteristic vertical to horizontal scales is not constant and can yield important information about physical scaling relationships. Spectral analysis is a hitherto under-utilised but powerful means to acquire statistical information about relevant amplitude and wavelength scales, simultaneously and with computational efficiency. Further, quantifying spatially distributed data in the frequency domain lends itself to the development of stochastic models for probing the underlying mechanisms which govern the spatial distribution of geological and geophysical phenomena. The software package `PySESA` (Python program for Spatially Explicit Spectral Analysis) has been developed for generic analyses of spatially distributed data in both the spatial and frequency domains. Developed predominantly in `Python`, it accesses libraries written in `Cython` and `C++` for efficiency. It is open source and modular, therefore readily incorporated into, and combined with, other data analysis tools and frameworks with particular utility for supporting research in the fields of geomorphology, geophysics, hydrography, photogrammetry and remote sensing. The analytical and computational structure of the toolbox is described, and its functionality illustrated with an example of a high-resolution bathymetric point cloud data collected with multibeam echosounder.

Keywords: point cloud, spectral analysis, geospatial analysis, roughness, texture, remote sensing

*Corresponding author

Email address: `dbuscombe@usgs.gov` (Daniel Buscombe)

1. Introduction

1.1. *The growing use of high-resolution point clouds in the geosciences*

Across a broad range of geoscience disciplines, interrogating the information in high-resolution spatially distributed data (point clouds) for the purposes of, for example, facies description and grain size calculation (e.g. Hodge et al., 2009; Nelson et al., 2014), geomorphic feature detection and classification (e.g. Burrough et al., 2000; Glenn et al., 2006; Pirotti and Tarolli, 2010), vegetation structure description (e.g. Antonarakis et al., 2009; Dassot et al., 2011), and physical habitat quantification (e.g. Vierling et al., 2008; Wheaton et al., 2010; Lassueur et al., 2006; Pradervand et al., 2014) has become increasingly widespread. The increasing accessibility and use of high-resolution topographic point clouds obtained using Light Detection and Ranging (LiDAR) (e.g. Buckley et al., 2008; Hilldale and Raff, 2008), Structure from Motion (SfM) photogrammetry (e.g. James and Robson, 2012; Westoby et al., 2012; Fonstad et al., 2013; Woodget et al., 2015), and range imaging (e.g. Nitsche et al., 2013) has found widespread application in geomorphology (Roering et al., 2013; Tarolli, 2014). The use of singlebeam and multibeam echosounders for bathymetric point cloud collection is on the ascendancy (Mayer, 2006) in geophysical and geomorphological research, and is becoming viable in increasingly shallow water (e.g. Parsons et al., 2005; Wright and Kaplinski, 2011; Buscombe et al., 2014b).

1.2. *Spatially explicit analysis of topographic point clouds*

With these technological developments, the heights of natural surfaces can now be measured with such spatial density that almost the entire spectrum of physical roughness scales can be characterised, down to the form and even grain scales (Brasington et al., 2012). Such ‘microtopography’ has created a demand for analytical and computational tools for spatially explicit (also known as spatially distributed) statistical characterization of the data (e.g. Keller et al., 1987; Church, 1988; Shepard et al., 2001; Manes et al., 2008; Pollyea and Fairley, 2011, 2012; Rychkov et al., 2012; Brasington et al., 2012; Trevisani et al., 2012; Kukko et al., 2013; Buscombe et al., 2014a). The basic premise is that the point cloud captures a surface whose statistical properties vary in space. Analysing data within small moving windows, calculating relevant statistics and spatially referencing them so they are represented in a decimated point cloud form, captures the spatial variability in the data and allows continuous mapping of statistical quantities such as roughness. This approach has found numerous applications in characterising rough surfaces (Smith, 2014). Of particular interest in roughness characterization is the extreme values, the width of the height distribution, or the length of the distribution tails. As such, the use of the root-mean-square (RMS) or standard deviation of heights (e.g. Shepard et al., 2001; Sankey et al., 2010; Nield et al., 2011) or amplitudes relative to a plane (Shepard et al., 2001; Frankel and Dolan, 2007; Pollyea and Fairley, 2011; Brasington et al., 2012) have become popular means to quantify surface roughness.

1.3. *A case for appropriate scaling of terrestrial roughness statistics*

The variance in amplitudes of a great many of geophysical quantities, including terrestrial surface heights, as a function of wavelength usually obeys a power law (Sayles and Thomas, 1978; Turcotte, 1992). An important consequence of power-law behaviour

44 is that RMS roughness, however defined, is scale-dependent (Sayles and Thomas, 1978;
45 Jackson and Richardson, 2007) and insufficient to discriminate between surfaces with
46 multiple roughness length scales. Despite this, the horizontal scale and spacing of rough-
47 ness elements is rarely considered (Smith, 2014) therefore the amplitude roughness is
48 rarely scaled by the horizontal spacing of amplitude deviations. The ratio of vertical
49 (e.g. standard deviation of heights) to horizontal (e.g. characteristic wavelength) scales
50 is rarely constant (Furbish, 1987). This suggests that the shape, orientation, inclination,
51 spacing and clustering of roughness ‘elements’ is important, as well as their vertical am-
52 plitude (Nikora et al., 1998; Pollyea and Fairley, 2012). These (non-amplitude) factors
53 give vital context to a given surface such as a streambed, seafloor, deflation surface,
54 outcrop or till fabric. In the terminology of fractals, rough surfaces are therefore called
55 ‘self-affine’ because a different scaling —called a Hurst number or Hausdorff exponent
56 —is required in the horizontal than in the vertical for them both to scale with each other
57 (Turcotte, 1992; Wilson and Dominic, 1998). A small Hurst number, for example, indi-
58 cates that a surface smooths disproportionately with increasing lengthscale (the surface
59 is rough up close and appears smooth at a distance). It is unlikely that terrestrial sur-
60 faces can be reliably distinguished from each other based on these scaling relationships
61 alone (Shepard et al., 2001). Measures of roughness are more physically meaningful if ex-
62 pressed as a parameter which scales vertical roughness to horizontal length characteristic
63 scales. In the geomorphologic sense, if ‘roughness’ is a measure of the statistical variation
64 in the distribution of topographic relief of a surface, then ‘texture’ can be defined as the
65 frequency of change and arrangement of roughness.

66 1.4. *Spatial explicit spectral analysis of point clouds*

67 Perhaps the most efficient and widespread means with which to simultaneously quan-
68 tify multi-scalar amplitudes and wavelengths in spatially distributed data, thereby simul-
69 taneously quantifying roughness and texture at multiple scales, is through application
70 of spectral analyses (e.g. Fara and Scheidegger, 1961; Gilman et al., 1963; Sayles and
71 Thomas, 1978; Hough, 1989; Perron et al., 2008; Hani et al., 2011; Trevisani et al., 2012).
72 Results of spectral analyses have the additional benefit of being amenable to theoretical
73 stochastic models of surface roughness, especially those that relate surface characteristics
74 to the scattering of light (Miller and Parsons, 1990; Whitehouse, 1997), radar (van Zyl
75 et al., 1991; Shepard et al., 1995) and sound (Jackson and Richardson, 2007).

76 Spectral analyses of spatially distributed data have proved beneficial for a number
77 of geophysical fields, including characterizing evolving topography (e.g. Cataño-Lopera
78 et al., 2009; Aberle et al., 2010; Singh et al., 2012), topographic feature extraction (e.g.
79 Lashermes et al., 2007; Booth et al., 2009; Passalacqua et al., 2010; Kalbermatten et al.,
80 2012; Berti et al., 2013), grain size analysis (Buscombe and Rubin, 2012; Buscombe, 2013)
81 and, classically, scaling and roughness of terrains (e.g. Rozema, 1968; Pike and Wes-
82 ley, 1975; Rothrock and Thorndike, 1980; Fox and Hayes, 1985; Family, 1986; Balmino,
83 1993). Spatially explicit analysis of lengthscales in data can also inform appropriate
84 spatial density of sampling (Pelgrum et al., 2000). Yet, in the catalogue of computa-
85 tional analytical tools now available to analyse the multiscale structures of geophysical,
86 geomorphological and remote sensing point cloud data, conspicuous in its absence are
87 accessible, open-source and generalised computational tools to describe the spatial con-
88 tinuity of the fields they represent and their internal correlations and spectral structures

89 (Wieland and Dalchow, 2009; Buscombe et al., 2014a). This paper addresses this short-
90 fall by 1) detailing the implementation of computationally efficient statistical analyses of
91 spatially distributed data such as point clouds and imagery, in the spatial and frequency
92 domains, in such a way that the resulting statistics are themselves spatially referenced
93 in a quasi-continuous sense (i.e. spatially explicit) as random fields of those statistical
94 quantities; and 2) describing a new open-source toolbox for generic point cloud analysis
95 which builds primarily on computational toolboxes for signal inference (Selig et al., 2013)
96 and terrestrial surface analysis (Rychkov et al., 2012).

97 **2. The PySESA program for spatially explicit analysis of point clouds**

98 *2.1. Scope and purpose*

99 PySESA stands for ‘Python program for Spatially Explicit Spectral Analysis’. Its field
100 of application is kept broad for a burgeoning interdisciplinary community and is therefore
101 not bound to a specific methodology or discipline. While PySESA might have immediate
102 application in the analysis of high-resolution topographic and bathymetric point clouds,
103 it also applies to a broad range of non-topographic, non-bathymetric, spatially-referenced
104 data. The use of acoustic backscatter, for example, is on the ascendancy for substrate
105 classification and bioacoustic detection (e.g. Anderson et al., 2008; Buscombe et al.,
106 2014b; Colbo et al., 2014). Similarly, optical backscatter such as LiDAR intensities (i.e.
107 reflectance of the LiDAR signal) is being used to facilitate terrestrial roughness and
108 land cover classifications (e.g. Pelgrum et al., 2000; Antonarakis et al., 2008; Franceschi
109 et al., 2009; Mallet and Bretar, 2009; Brodu and Lague, 2012; Trevisani et al., 2012), and
110 widespread use in volcanology (e.g. Mazzarini et al., 2007), and glaciology (e.g. Arnold
111 et al., 2006). Similar uses have been found for synthetic aperture radar (e.g. Crawford
112 et al., 1999), colours/intensities in the visible spectrum (e.g. Carbonneau et al., 2006;
113 Legleiter and Overstreet, 2012), or in fact any spatially referenced signal intensity in 3D
114 or 4D.

115 The input to the program is a (structured or unstructured) ‘point cloud’ of spatially
116 referenced amplitudes (elevation, depth, intensity, magnitude, etc) representing any two-
117 dimensional continuous function $Z = f(X, Y)$ where X and Y are horizontal coordinates
118 in a Cartesian mapping plane. Use of the term amplitude implies any relevant geophysical
119 quantity with a spatial reference in 2 or 3 dimensions. Point cloud data are simultaneously
120 analysed and decimated onto a regular grid. The output of the program is a set of
121 structured, decimated point clouds of a variety of output parameters. To do so, the
122 data are sub-divided into small windows of data with a specified degree of overlap and
123 according to a desired output grid spacing. Each window of data is analysed statistically
124 in either the spatial domain or frequency domain, or both. In a given window, all
125 computed quantities are spatially co-referenced at the centroid of the (X, Y) position of
126 that window.

127 *2.2. Implementation*

128 PySESA is a command-line program implemented in platform-independent object-
129 oriented Python¹ code, with computationally demanding procedural subroutines written

¹<https://www.python.org/>

130 in Cython² (Behnel et al., 2011) using C-style static type declarations which allows com-
131 pilation of static objects for efficiency. Python has become very popular for scientific
132 computing (Oliphant, 2007; Millman and Aivazis, 2011) because it is an open-source,
133 cross-platform, well-designed language with a clean syntax, a comprehensive standard
134 library, and an enormous worldwide user community with free access to third-party pack-
135 age repositories (such as PyPI³). It has the immediacy of a ‘scripting’ style language,
136 but also advanced capabilities such as easy interfacing with procedural languages (e.g.
137 C or Fortran) and other object-oriented languages (e.g. C++ and Java); parallelization;
138 graphics acceleration and distributed/cloud computing; web development; and static
139 compiling.

140 Numerical computations in PySESA are built around the efficiency of the NumPy⁴ array
141 (van der Walt et al., 2011), utilizing Cython’s support for fast access to NumPy arrays.
142 Additional numerical libraries are provided by SciPy⁵ (Jones et al., 2001–). Like recent
143 geological and geophysical Python toolboxes (e.g. Rushing et al., 2005; Wellmann et al.,
144 2012; Castelão et al., 2013; Krieger and Peacock, 2014) the design of PySESA is modular
145 which allows code readability, easy extension and adaptations in the future, and the
146 portability of its core functionality into other geospatial and geophysical analysis tools.

147 Operations on discrete windows of distributed data is highly amenable to so-called
148 ‘embarrassingly’ parallel (Foster, 1995) processing because different CPU threads can
149 access and process consecutive blocks of data stored in memory, without the need for
150 communication (and/or synchronization) between the different threads. In PySESA, par-
151 allelization of computational tasks is supported using the joblib⁸ library which allows
152 easy execution of tasks concurrently on (an automatically detected number of) separate
153 CPUs. Joblib also provides special handling for efficient processing of large Numpy
154 arrays by memory mapping using NumPy’s in-built memmap⁹ libraries.

155 2.3. Modules and typical workflow

156 Implementation and installation of PySESA is described in Appendix A and some
157 example uses are shown in Appendix B. Currently, PySESA consists of 7 main sub-modules
158 (`read` for reading data into the program; `partition` for windowing the data into discrete
159 portions of the input point cloud; `detrend` for detrending in the spatial domain and
160 filtering in the frequency domain; `spatial` for calculation of statistics in the spatial
161 domain; `spectral` for calculation of statistics in the frequency domain; `write` for writing
162 results to file; and `plot` for visualisation of outputs in a variety of ways and formats).
163 A list of all PySESA sub-modules (to date) and their functions is provided in Table 1. A
164 typical minimal workflow (Figure 1) and associated PySESA module is as follows:

- 165 • Read 3D point cloud data into program (`PySESA::read`) and specify user-inputs.
- 166 • Partition the point cloud into discrete windows of data (`PySESA::partition`) ac-
167 cording to user-specified inputs of output resolution, and degree of overlap between
168 windows.

²<http://cython.org/>

³<https://pypi.python.org/pypi>

⁴<http://www.numpy.org/>

⁵<http://www.scipy.org/>

⁸<http://pythonhosted.org/joblib/>

⁹<http://docs.scipy.org/doc/numpy/reference/generated/numpy.memmap.html>

- 169 • (Optional) Detrend or spatially filter each window of data (`PySESA::detrend`).
- 170 • Analyse each (detrended) point cloud window for a suite of user-prescribed spatial
171 (`PySESA::spatial`) and/or spectral (`PySESA::spectral`) parameters.
- 172 • Output results (`PySESA::write`).
- 173 • (Optional) Plot (`PySESA::plot`) results in a variety of ways, using `Matplotlib`⁶
174 (`Hunter, 2007`) and `Mayavi`⁷ (`Ramachandran and Varoquaux, 2011`) Python mod-
175 ules for two- and three-dimensional graphical visualisations.

176 3. Computational implementation

177 3.1. `PySESA::read`

178 The `read` module is highly optimised for reading ASCII files (comma, tab, or space
179 delimited) composed of three columns of numbers (with floating point precision) repre-
180 senting X , Y and Z , respectively. A file composed of 1 million 3D coordinates can be
181 read into memory in less than a second with an ordinary ≈ 2.5 GHz processor, and 10
182 million in less than 10 seconds.

183 3.2. `PySESA::partition`

184 Analyses are made spatially explicit by partitioning the 3D point cloud into small
185 windows of data, each of which are statistically analysed and the values of user-defined
186 parameters are assigned to the centroid location of each 3D data window. In a three-
187 dimensional region Ω consisting of points $\{P\}_{m=m_0}^M$ which is a subset of the entire point
188 cloud $P = [X, Y, Z]$ (i.e. $\{P\}_{m=m_0}^M \in P$), \mathbb{P}_m is defined as the set in Ω consisting of those
189 points in P which are within distance d of P_m :

$$\mathbb{P}_m = \mathbf{X} \in \Omega, \quad |\mathbf{X} - P_m| < |d|, \quad (1)$$

190 where two-dimensional vector $\mathbf{X} = (X, Y)$ and $m = m_0, \dots, M$. Given P with point
191 density ϵ , the centroids of \mathbb{P}_m are defined by (Buscombe and Rubin, 2012):

$$P_m^* = \frac{1}{|\mathbb{P}_m|} \int \mathbf{X} \epsilon(\mathbf{X}) \, d\mathbf{X}. \quad (2)$$

192 Here, the set of regions $\{\mathbb{P}_m\}_{m=m_0}^M$ are called ‘windows’ of P , and d and $\{P\}_{m=1}^M$
193 can be specified in such a way that the regions overlap to a specified degree. A com-
194 putationally highly efficient means to partition space as described above, with optional
195 overlap, is a nearest-neighbour search using the k-d (k-dimensional) tree (Bentley, 1975).
196 In `PySESA`, the efficient algorithm of Maneewongvatana and Mount (1999) is implemented
197 through `SciPy`’s `cKDTree`¹⁰ function. This approach to space partitioning, as opposed to
198 an alternative such as Voronoi tessellation (Buscombe and Rubin, 2012) or a two-pass
199 sorting procedure (Rychkov et al., 2012), enjoys the advantages associated with easy

⁶<http://matplotlib.org/>

⁷<http://docs.enthought.com/mayavi/mayavi/>

¹⁰<http://docs.scipy.org/doc/scipy/reference/generated/scipy.spatial.cKDTree.html>

200 specification of the degree of spatial smoothing (through the grid spacing and degree of
 201 overlap) in the final decimated grid. A useful feature of windowing like this is that limits
 202 can be imposed on M and m_0 , the maximum and minimum number of points considered,
 203 respectively, for each window.

204 3.3. *PySESA::detrend*

205 Detrending is high-pass filtering in the spatial domain through the subtraction of a
 206 1) mean, 2) least-squares plane, or 3) modelled surface, from the amplitude data so the
 207 small-scale variations are emphasized and the large-scale trends are removed (Brasington
 208 et al., 2012). All three approaches described above are implemented in *PySESA* (Figure
 209 3). A detrending operation is a necessary pre-processing step prior to spectral analysis.
 210 Another motivation to detrend each window of data is that, as argued by Brasington et al.
 211 (2012) and Pollyea and Fairley (2011), the standard deviation of amplitudes relative to
 212 a local plane fit through the data is a more powerful statistical descriptor of amplitude
 213 roughness compared with standard deviation of \mathbb{P}_m , because it emphasises the smallest
 214 scale amplitude variance relative to the local mean amplitude (Figure 4).

215 Below, the detrended windowed point cloud is denoted $\widehat{\mathbb{P}}_m$. *PySESA* supports three
 216 types of plane fitting (Figure 3), those based on: 1) ordinary least squares (OLR) (e.g.
 217 Rychkov et al., 2012); 2) robust linear model (RLM); and 3) orthogonal distance regres-
 218 sion (ODR) (e.g. Pollyea and Fairley, 2011). Given the plane through the unstructured
 219 point cloud \mathbb{P}_m , given by

$$aX + bY + c = 0, \quad (3)$$

220 the normal vector to the plane is

$$\mathbf{v} = \nabla f = \begin{bmatrix} a \\ b \\ c \end{bmatrix}. \quad (4)$$

221 Ordinary and robust linear regression are implemented using routines provided by the
 222 `statsmodels`¹¹ package. In ordinary linear regression, the sum of the squared vertical dis-
 223 tances between the \mathbb{P}_m data values and the corresponding \mathbb{P}_m values on the fitted plane
 224 are minimized to find \mathbf{v} . Robust linear models do the same via iteratively reweighted least
 225 squares and given the robust criterion estimator detailed in Huber (1981). In orthogonal
 226 distance regression (Boggs et al., 1992), \mathbf{v} is found by minimizing the orthogonal (per-
 227 pendicular) point-to-plane distances, d_i , given by projecting the vector from the plane
 228 to an arbitrary point $(x_0, y_0, \widehat{\mathbb{P}}_m)$ onto \mathbf{v} , a line normal to the plane

$$d_i = \frac{|aX_0 + bY_0 + \mathbb{P}_{m0} + c|}{\sqrt{a^2 + b^2 + 1}}. \quad (5)$$

229 In *PySESA*, this is computed using *SciPy* wrappers to the *ORDPACK*¹² library (Boggs
 230 et al., 1992) and a custom numerical procedure by which coefficients \mathbf{v} from an ordinary
 231 least squares model are used as initial estimates for \mathbf{v} for a more accurate fit. For very
 232 large point cloud windows, the implicit minimization of equation 3 can be speeded up
 233 considerably by pre-computing its derivatives using Jacobian functions during the fitting.

¹¹<http://statsmodels.sourceforge.net/>

¹²<https://docs.scipy.org/doc/scipy-0.15.1/reference/odr.html>

234 *3.4. PySESA::spectral*

235 *3.4.1. Gridding*

236 Gridding is the process that converts an unstructured detrended window of point
237 cloud, $\widehat{\mathbb{P}}_m$, to a structured random field, $\mathbb{P}_m(\mathbf{X}_m)$, defined over the regular grid \mathbf{X}_m
238 composed of square grid cells, and specified by the joint probability density function
239 $p(\mathbb{P}_m(\mathbf{X}_{m1}), \mathbb{P}_m(\mathbf{X}_{m2}), \dots : \mathbf{X}_{m1}, \mathbf{X}_{m2}, \dots \in [X_m, Y_m])$. $\mathbb{P}_m(\mathbf{X}_m)$ consists of $N_{X_m} \times$
240 N_{Y_m} observations at regular intervals $\Delta X_m = \Delta Y_m$ and is achieved using the SciPy
241 routine `griddata`¹³. Nearest-neighbour interpolation (which returns the value at the
242 data point closest to the point of interpolation) is used by default, but linear and cubic
243 interpolation is also possible (with an associated loss in computational speed, and at
244 the risk of introducing artificial autocorrelation into the data). Note that this process is
245 required for spectral analyses only: descriptive statistics (section 3.8) are calculated on
246 unstructured point clouds.

247 *3.4.2. Spatial Domain Filtering (with PySESA::sgolay)*

248 PySESA implements the Savitzky-Golay low-pass filter (Savitzky and Golay, 1964) in
249 2D (Figure 3d) to provide the option of spatial domain filtering of $\mathbb{P}_m(\mathbf{X}_m)$ prior to
250 spectral analysis. This can be used to low-pass filter the data or, through subtraction of
251 the filter from the data, high-pass filter. As the latter, the Savitzky-Golay filter can also
252 be used as a higher-dimensional detrending surface model which can be subtracted from
253 the data instead of a 2D plane. As such, it is optionally called by the `detrend` module.

254 The idea behind Savitzky-Golay filtering is to find filter coefficients that preserve
255 higher moments in the data. Filters such as a moving average preserve the zeroth moment
256 of a spectrum but violate the 2nd moment. The underlying function in a Savitzky-Golay
257 approach is approximated within a moving window by a polynomial of higher order,
258 typically quadratic or quartic, rather than a constant. For each point $p(x_m, y_m)$ of
259 $\mathbb{P}_m(\mathbf{X}_m)$, a window centred at that point is extracted, a least-square fit of a polynomial
260 surface is computed, and the initial central point is replaced with the value computed
261 by the fit. In PySESA, the coefficients are pre-computed for efficiency (using convolution
262 routines) because they are linear with respect to the data spacing (Press et al., 2007).
263 Evaluation of the fit at the borders of the data is achieved by padding the convolved
264 data with a mirror image of the data.

265 *3.4.3. Power Spectrum*

266 The power spectrum $\Psi_2(\mathbf{K})$ (with dimensions length^4), or equivalently its Fourier
267 transform, the autocorrelation function $\xi_2(\mathbf{L})$ (over \mathbf{L} lags) is a measure of the variance
268 of amplitudes in $\mathbb{P}_m(\mathbf{X}_m)$ associated with different narrow bands of unit $\mathbf{K} = (k_X, k_Y)$,
269 which is a two-dimensional wave vector (whose magnitude $K = \sqrt{k_X^2 + k_Y^2} = 2\pi/\lambda$
270 is the wavenumber, λ being the wavelength) related to the frequency components by
271 $F_X = \frac{k_X}{N_X \Delta X}$ and $F_Y = \frac{k_Y}{N_Y \Delta Y}$. Therefore, the wavenumber describes the number of
272 times the function $\mathbb{P}_m(\mathbf{X}_m)$ has the same phase per unit space.

273 To prevent spectral leakage during the estimation of $\Psi_2(\mathbf{K})$, $\mathbb{P}_m(\mathbf{X}_m)$ is first tapered
274 by multiplying with a 2D taper $T(i, j)$. Then $\Psi_2(\mathbf{K})$ is normalized to account for the
275 change in variance associated with the application of the taper (Buscombe et al., 2014a).

¹³<http://docs.scipy.org/doc/scipy/reference/generated/scipy.interpolate.griddata.html>

276 Generic 2D tapering in PySESA is achieved using the vectorised method detailed in Ap-
277 pendix C.

278 Power spectral density estimation in PySESA is carried out using NIFTy¹⁵ libraries
279 (Selig et al., 2013), capitalizing on the NIFTy `rg.space`¹⁶ class, which allows computa-
280 tionally efficient transformation between regular grid and wavenumber spaces. Power
281 spectral density smoothing in the frequency domain is also carried out using NIFTy which
282 implements the algorithms of Enßlin and Frommert (2011) and Oppermann et al. (2013).
283 This process is detailed in Appendix D.

284 The 1D marginal spectrum, $\Psi_1(\mathbf{K})$, is the 2D spectrum collapsed as a function of the
285 radial wavenumber $\mathbf{K} = \sqrt{K_X^2 + K_Y^2}$. The subscript 1 here, and elsewhere below, denotes
286 calculations based on the 1D form of the spectrum. No radial integration occurs, therefore
287 this spectral form incorporates any anisotropy (directional dependence) in $\mathbb{P}_m(\mathbf{X}_m)$. If
288 this is a concern for any reason, the user must choose a window size that ensures the
289 spectrum is isotropic.

290 3.4.4. Background Estimation

291 Given the power-law form of $\Psi_1(\mathbf{K})$, the background spectrum, $\overline{\Psi_1(\mathbf{K})}$, is a version
292 of the spectrum in which there is no concentration of variance in any wavenumber band.
293 Comparison between $\Psi_1(\mathbf{K})$ and $\overline{\Psi_1(\mathbf{K})}$ allows identification of deviations in $\Psi_1(\mathbf{F})$ and
294 therefore any statistically significant periodicities in the data. A bin-averaging approach
295 to estimating $\overline{\Psi_1(\mathbf{K})}$ is biased by the peaks and troughs in the spectrum, therefore a
296 preferable approach is to construct a simulated surface with identical global, but different
297 local, statistics (Perron et al., 2008). In PySESA, this is achieved by simulating Gaussian
298 2D random field drawn from $\Psi_2(\mathbf{K})$ using the methods detailed in Oppermann et al.
299 (2013) and summarised briefly in Appendix E, then collapsed as a function of \mathbf{K} to give
300 $\Psi_1(\mathbf{K})$.

301 This simulated field is statistically homogeneous and isotropic, which means the cor-
302 relation between two field values at two positions depends only on their physical distance
303 ($|\mathbf{X}_{m=1} - \mathbf{X}_{m=2}| \propto 1/\mathbf{K}$). $\overline{\Psi_1(\mathbf{K})}$ is therefore a smooth spectral approximation to an
304 isotropic form of $\Psi_2(\mathbf{K})$ and has the same covariance as $\mathbb{P}_m(\mathbf{X}_m)$. This covariance
305 captures the essential features of low-frequency variation over relatively large separation
306 distances, but the spectra $\Psi_1(\mathbf{K})$ and $\overline{\Psi_1(\mathbf{K})}$ diverge at higher frequencies because $\overline{\Psi_1(\mathbf{K})}$
307 doesn't contain the information on either large changes in amplitude over short distances
308 (Sayles and Thomas, 1978) or asymmetry about a vertical or horizontal axis, because is
309 unaffected by a change in sign of $\Psi_{k=1} - \Psi_{k=2}$ or $\mathbf{X}_{m=1} - \mathbf{X}_{m=2}$ (Goff and Jordan, 1988).

310 3.5. Integral lengthscale (with `PySESA::lengthscale`)

311 The autocorrelation function is the normalised covariance between the signal and
312 itself when offset by some lag, and exhibits periodicity —where present— at the same
313 period as the original signal. In PySESA, the autocovariance function $\xi_2(\mathbf{L})$, over \mathbf{L} lags,
314 is calculated as the 2D continuous Fourier transform of $\Psi_2(\mathbf{K})$ (Priestley, 1981) then
315 integrated radially over segments to collapse it to 1D:

¹⁵<http://www.mpa-garching.mpg.de/ift/nifty/index.html>

¹⁶http://www.mpa-garching.mpg.de/ift/nifty/base_space.html

$$\xi_1(\mathbf{L}) = \int_0^{2\pi} \mathcal{F}[\Psi_2(\mathbf{K})](\mathbf{K} \cos \theta, \mathbf{K} \sin \theta) \mathbf{K} d\theta, \quad (6)$$

where θ is a vector of equal-area sectors subtended by a given angle centred in the DC component in frequency space, over which the radial integration occurs. It is assumed that the radial integration incorporates any significant anisotropy in $\mathbb{P}_m(\mathbf{X}_m)$.

The definition of the integral length-scale, l_0 , comes originally from turbulence research (Taylor, 1938) as a measure of some relatively large lag over which the the auto-correlation converges to zero, indicative of the largest turbulent eddy scale. The same principle applies to spatially distributed data if fluctuating velocity in time is replaced by fluctuating amplitude in space (c.f. Nikora, 2005). Strictly speaking, l_0 is the product of 2π and the spectral amplitude at $\mathbf{K}=0$ (Taylor, 1938) however evaluation of this amplitude would require an infinitely long spatial series. A pragmatic approach is to pick the lag to which, when integrated to, the correlation equals zero (beyond which only harmonics remain, whose correlations by definition are harmonics at the same wavenumber), or:

$$l_0 = \int_{\mathbf{L}_0} \xi_1(\mathbf{L}) d\mathbf{L}, \quad (7)$$

with \mathbf{L}_0 defined as either the lag to which ξ_1 falls to zero (Taylor, 1938), the product of 2π and the lag at which ξ_1 falls to half its value at zero lag (Buscombe et al., 2010), or the lag required to reduce ξ_1 to $1/e$ (Shepard et al., 2001). All three methods for calculating the integral lengthscale are common and provided in PySESA and it is left as an exercise to the interested reader to examine how these measures relate for different point clouds.

In general, smoother surfaces have larger integral lengthscales. However, the concepts behind this statistical measure have been used to describe how variance in various geophysical phenomena cascades (dissipates, or ‘smears’ (Jerolmack and Paola, 2010)) across spatial scales (Guadagnini and Neuman, 2011), in which case large integral lengthscales could also indicate slow ‘dissipation’ rates from variance associated with small wavelengths to variances associated with larger wavelengths in the data.

3.5.1. Slope and intercept

Spectral power of distributed spatial data decreases rapidly with increasing frequency (Shepard et al., 2001). This power-law behaviour cannot persist at very high frequencies, which leads to spectral ‘roll over’ where the spectral slope steepens (Priestley, 1981). The length scale associated with this rollover frequency is the outer scale L_0 , which is assumed in PySESA to be the point of divergence between $\Psi_1(\mathbf{X}_m)$ and the background power spectrum $\widehat{\Psi}_1(\mathbf{K})$. A simple functional form of $\Psi_1(\mathbf{K})$ is a power-law (von Karman and Howarth, 1938):

$$\widehat{\Psi}_1(\mathbf{K}) = \frac{\omega_1}{(h_0|\mathbf{K}|)^{\gamma_1}}, \quad \frac{2\pi^{-1}}{\mathbf{K}} > 1/L_0, \quad (8)$$

The inclusion of a dimensional constant, h_0 , in equation 8 allows ω_1 to have dimensions length^4 , independent of the value of non-dimensional γ_1 (Jackson and

351 Richardson, 2007). Spectral strength and exponent are estimated from bin averages of
 352 the marginal power spectrum $\Psi_1(\mathbf{K})$, as the parameters that minimize the error

$$\|(\gamma_1 \mathbf{K}_b + \omega_1) + \widehat{\Psi}_{1b}\|^2, \quad \mathbf{K}_b = \frac{2\pi^{-1}}{\mathbf{K}} > 1/L_0, \quad (9)$$

353 where $\|$ represents the 2-norm and subscript b denotes bin average. Appendix F details
 354 the parameter estimation. As well as γ_1 and ω_1 , the correlation coefficient of the regres-
 355 sion, the two-sided p-value for a hypothesis test whose null hypothesis is that the slope
 356 is zero, and the standard error of the slope coefficient estimate ($= \sqrt{MSE/\sigma_{\mathbf{K}_b}}$ where
 357 MSE is a mean square error —the sum of squared residuals divided by number of model
 358 parameters —and $\sigma_{\mathbf{K}_b}$ is the variance in the independent variable) are also calculated.
 359 Since γ_1 is always negative, an estimate of fractal dimension is then $D = (8 + \gamma_1)/2$
 360 (Huang and Turcotte, 1990; Perron et al., 2008).

361 The spectral strength, ω_1 , is a measure of power at low frequencies, or the magnitude
 362 of signal fluctuations over relatively large spatial distances. The spectral exponent, γ_1 ,
 363 is a measure of the rate of decay in signal power as a function of increasing frequency.
 364 The more complex the spatial patterns in the data, the greater range of frequencies must
 365 be used to describe it. Therefore, γ_1 is a useful measure of how complex the data is by
 366 quantifying the range of frequencies necessary to describe the data.

367 3.6. Amplitude and length scales

368 The area under the power spectral density curve is equal to the variance of the
 369 amplitude distribution (Sayles and Thomas, 1978). For normally distributed amplitudes,
 370 σ_1 is equivalent to the root-mean-square amplitude, which in PySESA is calculated as:

$$\sigma_1 = \sqrt{\int_{\mathbf{K}_0} \Psi_1(\mathbf{K}) d\mathbf{K}}, \quad \frac{2\pi^{-1}}{\mathbf{K}_0} = \frac{2\pi^{-1}}{\mathbf{K}} > 1/L_0, \quad (10)$$

371 in which the definite integral is estimated using the composite trapezoidal method (SciPy's
 372 `trapz` function). σ_1 is a measure of the magnitude of signal fluctuations over all space
 373 (both large and small separation distances) and is therefore only pertinent to roughness,
 374 not texture, which is better quantified by measures of dominant wavelengths in the data.
 375 PySESA calculates peak wavelength as:

$$\lambda_{peak} = \left(\frac{2\pi}{\mathbf{K} \left[\operatorname{argmax} \left(\Psi_1(\mathbf{K}) / \Psi_1(\mathbf{K}) \right) \right]} \right) d\mathbf{X}, \quad (11)$$

376 which can only take on discrete values. A more continuously distributed measure of
 377 central tendency in wavelength is also calculated:

$$\lambda_{mean} = \int_{K_0} \left(\frac{\Psi_1(\mathbf{K})}{\Psi_1(\mathbf{K})} \right) 2\pi^{-1} d\mathbf{X}, \quad \frac{2\pi^{-1}}{\mathbf{K}_0} = \frac{2\pi^{-1}}{\mathbf{K}} > 1/L_0. \quad (12)$$

378 The ratio of the RMS roughness (equation 10) to the integral lengthscale gives the
 379 ‘effective slope’ (Campbell and Garvin, 1993; Shepard et al., 2001), expressed in degrees:

$$\phi = \tan^{-1} \left(\frac{\sigma_1}{l_0} \right). \quad (13)$$

380 *3.7. Moments and Spectral Width*

381 PySESA provides the means to calculate a number of useful quantities from the mo-
 382 ments of the power spectrum $\Psi_1(\mathbf{K})$, defined as:

$$m_k = \int_0^\infty \mathbf{K}^k |\Psi_1(\mathbf{K})|^2 d\mathbf{K}, \quad (14)$$

383 which says that the content at every frequency in the spectrum is weighted by the k th
 384 power of the frequency and the result is summed up across the entire spectrum. The
 385 power in the signal is m_0 . The moment of inertia around the axis $\mathbf{K}=0$ is m_2 . Since the
 386 bandwidth of the signal is $\sigma_m = \sqrt{m_2/m_0}$, the number of zero crossings per unit space is
 387 given by $N_0 = 2\sqrt{m_2/m_0}$. The derivative of $\mathbb{P}_m(\mathbf{X}_m)$ has the marginal power spectrum
 388 $|2\pi\mathbf{K}\Psi_1(\mathbf{K})|^2$ and the bandwidth $\sqrt{m_4/m_2}$, therefore the number of extrema per unit
 389 space is $E_0 = 2\sqrt{m_4/m_2}$. Two measures of the average wavenumber are $\lambda = m_0/m_1$
 390 and $\lambda = \sqrt{m_0/m_2}$. The spectral width is a dimensionless parameter which describes the
 391 way in which spectral area is distributed around the mean wavenumber. Two measures
 392 of spectral width are implemented in PySESA: 1) $\nu = \sqrt{1 - m_2^2/m_0m_4}$ (Cartwright and
 393 Longuet-Higgins, 1956) which approaches zero as the spectrum becomes more narrow
 394 banded; and 2) the ‘normalised radius of gyration’, or $\nu = \sqrt{(m_0m_2/m_1^2) - 1}$ (Longuet-
 395 Higgins, 1975) which doesn’t rely on the fourth spectral moment, so is numerically more
 396 stable.

397 *3.8. PySESA::spatial*

398 PySESA is predominantly a library for spectral analyses but also implements operations
 399 for calculation of descriptive statistics (standard deviation, skewness, and kurtosis) on
 400 point clouds in the spatial domain. Root-mean-square (RMS) height, or the standard
 401 deviation of amplitudes about the mean, is the square root of the variance of amplitudes

$$\sigma^2 = \left\langle \left(\mathbb{P}_m(Z) - \overline{\mathbb{P}_m(Z)} \right)^2 \right\rangle, \quad (15)$$

402 or detrended amplitudes

$$\sigma_d^2 = \left\langle \left(\widehat{\mathbb{P}_m}(Z) - \overline{\widehat{\mathbb{P}_m}(Z)} \right)^2 \right\rangle. \quad (16)$$

403 Sample variance, skewness and kurtosis are calculated using the numerically stable
 404 method of Welford (1962) as implemented by Knuth (1998) and discussed by Chan et al.
 405 (1983). This method is less prone to loss of precision in floating point arithmetic due to
 406 subtracting two nearly equal numbers, which is especially important when calculating the
 407 variance of small residuals of points relative to a plane. Large errors in compiled statistics
 408 can result otherwise. The Welford-Knuth algorithm is written in C++ and compiled into a
 409 Python module using the SWIG¹⁷ interface compiler (Beazley, 2003). The ‘effective slope’
 410 (ratio of the RMS roughness to the integral lengthscale) can be calculated in the spatial
 411 domain using equation 13.

¹⁷www.swig.org/exec.html

412 4. Demonstration

413 In order to demonstrate the functionality of the PySESA toolbox, a bathymetric point
414 cloud of a 60×80 m patch of the Colorado River bed in Western Grand Canyon (Figure
415 5), around river mile 224 (approximately 360 km downstream of Lees Ferry, Arizona,
416 USA) was analysed. The point cloud was obtained using multibeam echosounder, is
417 composed of almost 1 million 3D points (at a density of around 200 points per square
418 metre). Details on the methods for acquisition and analysis of such data in this environ-
419 ment are found in Kaplinski et al. (2009, 2014), Grams et al. (2013) and Buscombe et al.
420 (2014a). Most important for the present purposes is that the point cloud clearly shows
421 areas of varying textures and roughnesses, including sand dunes with a quasi-regular
422 crest spacing, relatively flat sand areas, and relatively high elevation rocky areas. The
423 point cloud was analysed for all spatial and spectral parameters using a 0.25×0.25 m
424 regular output grid spacing with 0% overlap. Each window contained a minimum of 64
425 data points. A ODR plane was used to detrend data in each window. Prior to spectral
426 analysis, the data were Hann tapered.

427 The decimated output point cloud shown in Figure 6a has been colour-coded by
428 spectral root-mean-square variation in amplitude, σ_1 (m) (equation 10). As expected,
429 roughness is high (light colours) in the rocky areas, intermediate in the dune field, and
430 low in the flatter areas in between. The same cloud of points in Figure 6b has been
431 colour-coded by spectral strength ω_2 (m^4) (equation 9). To recap from section 3.5.1, the
432 spectral strength, ω_1 , is a measure of power at low frequencies. Rocky areas therefore
433 have relatively low values of spectral strength because the magnitude of topographic
434 fluctuations over relatively large spatial distances is small compared to those over short
435 distances. The potential for automated physically-based segmentation of different ge-
436 omorphic units (dunes, flat sand and rocks) is apparent in this case and would have
437 enormous potential application in, for example, channel bed physical habitat character-
438 isation and sediment transport studies. To further illustrate this point, contour maps
439 of various gridded parameters, which are a selection of those resulting from spatial and
440 spectral analyses of the point cloud shown in Figure 5 are shown in Figure 7. In each
441 subplot, just a small 70×45 m portion of the data is shown. Spectral strength (Figure
442 7b), spectral width (Figure 7e), ODR detrended standard deviation (Figure 7f) and ratio
443 of integral lengthscale and RMS roughness (Figure 7i) would be particularly effective pa-
444 rameters by which to delineated rocky, flat and rough sand areas. Other parameters such
445 as the non-detrended standard deviation (Figure 7f) and integral lengthscale (Figure 7d)
446 seem likely to be able to delineate dune crests from troughs.

447 Similar analyses could find particular utility in, for example, automated landscape,
448 soil or vegetation classification or segmentation of natural textures in remote sensing im-
449 agery; seafloor substrate mapping and benthic habitat characterisation using multibeam
450 data; or spatially explicit mapping of grain size and roughness variations in streambeds,
451 surficial geology, lava flows or vertical sedimentary sequences using LiDaR or high-
452 resolution imagery, among many other uses.

453 5. Discussion and future developments

454 According to Trevisani et al. (2012) and Berti et al. (2013), an ideal algorithm for a
455 spatially explicit analysis of surfaces should:

- 456 (1) provide a pixel-by-pixel characterisation of the surface;
- 457 (2) run on large datasets with a computational and memory efficiency;
- 458 (3) measure an intrinsic property of the surface, invariant with respect rotation or
- 459 translation;
- 460 (4) take into account scale dependency; and
- 461 (5) have an intuitive or physical meaning.

462 It is instructive to evaluate the PySESA toolbox against these criteria. (1) doesn't
 463 strictly apply because geospatial data are analysed as point clouds rather than gridded
 464 surfaces, however information from each measured location in the point cloud is utilized.
 465 There is no interpolation across space: if there is no data in a particular grid location, or
 466 not enough data (defined by the `min_pts` parameter to the `partition` module), there are
 467 no outputs at that location. The spatial density of results (degree of decimation) depends
 468 on the (user-defined) scale at which the outputs are meaningful, and the processing time
 469 (related to the size of the cloud) deemed acceptable.

470 Regarding (2), special attention has been paid to making the program computation-
 471 ally efficient (within the constraints of using an interpreted language) using statically
 472 compiled subroutines which run in parallel. So far, the program has been used on up to
 473 and including $\mathcal{O}(10^7)$ point clouds. More work is required to make the program memory
 474 efficient enough to process point clouds of $\mathcal{O}(10^8)$ or more. The program would run with
 475 only minor modifications on high performance computing environments. The combina-
 476 tion of a one-time binary-tree (k-d tree) space partition, with a computational complexity
 477 $\mathcal{O}(n \log n)$, to sort the point cloud into windows, then successive application of the FFT
 478 algorithm, each with a computational complexity $\mathcal{O}(n \log n)$, on each window, results in
 479 an overall computational cost of $\mathcal{O}(n^2)$ to analyse each point cloud. Therefore the overall
 480 processing time as a function of the number of points in the cloud is quasi-linear in log-log
 481 space (Figure 8) and doubling the number of processors over which the computations are
 482 handled results in a $\approx 50\%$ speedup (Figure 9).

483 Metrics calculated using Fourier methods are not inherently invariant with respect to
 484 rotation or translation (3). However, because small windows are used in the processing;
 485 because detrending can be applied; and because spectral metrics computed in PySESA
 486 are based on 2D spectra which are then collapsed (not radially averaged) to a 1D form;
 487 any anisotropy is incorporated. The one caveat to that statement would be for coarse
 488 output grids. How coarse is too coarse depends on the degree of anisotropy in a typical
 489 data window. In choosing an appropriate window size (a function of output spacing and
 490 overlap), there is a trade-off between a size small enough to ensure data in a typical
 491 window are isotropic, yet large enough to preserve required detail in the outputs at an
 492 acceptable statistical power (related to N). The effects of window size and degree of
 493 window overlap would vary on the degree of spatial variability in the data, and on the
 494 specific output parameter. Those parameters quantifying lengthscales (e.g. λ_{mean} and
 495 l_0) are most susceptible to choice of window size, but large window sizes also affect
 496 measures of amplitude (e.g. σ_1 , σ and σ_d) if amplitudes are strongly varying across the
 497 window such that mean or plane detrending has a diminished effect of amplifying local
 498 variations in amplitude relative to the mean amplitude. Window overlap controls the
 499 degree of spatial smoothing in the outputs and therefore its effects on output parameters
 500 is hard to predict.

501 On (4), as discussed in section 1.3, spectral methods provide the means to calculate
502 horizontal (e.g. λ_{mean} and l_0) and amplitude (e.g. σ_1) scaling and the scaling between
503 them (such as D and ϕ). Finally, regarding (5), all measures calculated by the PySESA
504 (summarised in Table 1) have physical connotations (indeed, most have physical units),
505 being related to either the amplitude or horizontal lengthscales of signal fluctuations
506 or measures describing the distribution of amplitudes in the spatial (e.g. skewness and
507 kurtosis) or frequency (e.g. m_k and ν) domains.

508 PySESA could be extended by inclusion of frequency domain filtering and bandwidth
509 specification which would allow the user to specify a range of wavenumbers over which
510 to calculate the power spectrum. In addition, co-variance and co-spectra of 4D data
511 (two dependent amplitudes variables co-registered in space) such as lidar intensities and
512 elevations, or sonar backscatter amplitudes and depths, could be calculated. Finally, the
513 toolbox could be easily extended to include spatial analogs to the power spectrum such
514 as variograms and structure functions.

515 Acknowledgements

516 This work was funded by the Glen Canyon Dam Adaptive Management Program
517 administered by the U.S. Bureau of Reclamation. Any use of trade, product, or firm
518 names is for descriptive purposes only and does not imply endorsement by the U.S.
519 government. Thanks to Matt Kaplinski, Erich Mueller and Bob Tusso for helping collect
520 the field data, and Paul Grams for helpful discussions.

521 Appendix A. Implementation and installation

- 522 • PySESA is completely open source and has been developed under a GNU General
523 Public License. The project homepage is [http://dbuscombe-usgs.github.io/
524 pysesas/](http://dbuscombe-usgs.github.io/pysesas/) which provides documentation and further analysis examples.
- 525 • The program requires NumPy, SciPy, Cython, matplotlib, NIFTy, joblib, and statsmodels
526 modules. A `setup.py distutils`¹⁸ script is provided to automatically install these
527 dependencies.
- 528 • The program is available on the Python package repository ([https://pypi.python.
529 org/pypi/pysesas](https://pypi.python.org/pypi/pysesas)) and can be installed from the command line using: `pip install
530 pysesas`.
- 531 • The ASCII format is used for both input and outputs, despite the overhead involved
532 in textural conversions and the sequential nature of I/O operations, for maximum
533 compatibility with other software. Support for other, more efficient, binary formats
534 (such as LAS, netCDF and HDF) will be implemented in the future to the `read`
535 module.

¹⁸<https://docs.python.org/2/distutils/>

- 536 • PySESA has a `git` version-control backend and is freely available on the `github`[®]
537 online repository: <https://github.com/dbuscombe-usgs/pyseses> which allows
538 centralised storage and customization by users (‘forking’) through development
539 branches (‘forks’). Additions of new functions and sub-modules can be made or
540 incorporated into other software tools by interested developers.
- 541 • Each function is annotated with `docstrings` explaining functionality and syntax,
542 which can be accessed within python using `module.__doc__`, or using the `module?`
543 syntax in `ipython`¹⁹.
- 544 • `sphinx`²⁰ has been used to generate html web pages for the project. These can be
545 compiled locally using the supplied Makefile (`make html`) or batch (`make.bat`) file
546 on Windows[®].
- 547 • So far the program has been tested with Python version 2.7, on various distributions
548 of Linux and Windows[®] 7.

549 Appendix B. Example usages of PySESA

550 The submodule `PySESA::process` allows full control over all types of workflows through
551 use of a number of processing flags. A minimum working example usage of the the `PySESA`
552 module, accepting all default values for parameters, is:

```
553 import pysesa
554 infile = '/home/me/mypointcloudfile.txt'
555 pysesa.process(infile)
```

556 This instance writes out the following results file whose name contains some of the
557 processing parameters:

```
558 /home/me/mypointcloudfile.txt_zstat_detrend4_outres0.5_proctype1_mxpts512_minpts16.xyz
```

559 The above is the same as passing a list of default-valued variables to `PySESA::process`,
560 which is included for completeness in the `PySESA::test` module:

```
561 out = 1 # 1 m output grid
562 detrend = 4 # detrend type: ODR plane
563 # Processing type: spectral parameters (no smoothing) only
564 proctype = 1
565 mxpts = 1024 # Maximum points per window
566 # 5 cm grid resolution for detrending and spectral analysis
567 res = 0.05
568 nbin = 20 # Number of bins for spectral binning
569 lentype = 1 # Integral lengthscale type: 1<0.5
570 taper = 1 # Hann taper before spectral analysis
571 prc_overlap = 0 # No overlap between successive windows
572 minpts = 64 # Minimum points per window
573
574 pysesa.process(infile, out, detrend, proctype, mxpts, res, nbin, lentype, minpts, taper, prc_overlap)
```

¹⁹<http://ipython.org/>

²⁰<http://sphinx-doc.org/latest/index.html>

575 A minimal example analysis of spatial and spectral analysis on just 1 window of data:

```
576 # import module
577 import pysesa
578
579 # read point cloud from file
580 pointcloud = pysesa.read.txtread(infile)
581
582 # create windows of data
583 windows = pysesa.partition(pointcloud).getdata()
584
585 # process window number 50
586 k=50
587
588 # get all spectral statistics for that window
589 spec_stats = pysesa.spectral(
590 pointcloud[windows[k],:3].astype('float64')).getdata()
591
592 # get all spatial statistics for that window
593 spat_stats = pysesa.spatial(
594 pointcloud[windows[k],:3].astype('float64')).getdata()
595
```

596 and to extend this to all windows, utilising parallel processing over all available cores,
597 could be achieved using the following minimal example:

```
598 # define a function that will get repeatedly
599 # read by the parallel processing queue
600 def get_spat_n_spec(pts):
601     return pysesa.spatial(pts.astype('float64')).getdata()
602 + pysesa.spectral(pts.astype('float64')).getdata()
603
604 # import the parallel processing libraries
605 from joblib import Parallel, delayed, cpu_count
606
607 # Processing type: spatial plus spectral
608 #parameters (no smoothing)
609 proctype = 4
610
611 # process each window with all available cores,
612 # by queueing each window in a sequence
613 # and processing until they are all done
614 w = Parallel(n_jobs=cpu_count(), verbose=0)
615 (delayed(get_spat_n_spec)(pointcloud[windows[k],:3])
616 for k in xrange(len(windows)))
617
618 # parse out the outputs into variables
619 x, y, z_mean, z_max, z_min, z_range, sigma, skewness, ...
620 kurtosis, n, slope, intercept, r_value, p_value, ...
621 std_err, d, l, wmax, wmean, rms1, rms2, Z, E, ...
622 sigma, T0_1, T0_2, sw1, sw2, m0, m1, m2, ...
623 m3, m4, phi = zip(*w)
```

624 To obtain just the integral lengthscale of the *k*th window, detrended using the or-
625 thogonal distance regression detrending technique, one could use:

```
626 detrend = 4 # Orthogonal distance regression
627 pysesa.lengthscale(pysesa.detrend(
628 pointcloud[windows[k],:3],detrend).getdata()).getlengthscale()
```

629 and to get the spatial statistics from the same data:

```
630 pysesas.spatial(pysesas.dettrend(  
631 pointcloud[windows[k],:3],dettrend).getdata()).getdata()
```

632 In this final example, the output grid resolution is changed to 25 cm, and the various
633 outputs from the `spectral` module are obtained separately:

```
634 # 25 cm output grid  
635 out = 0.25  
636  
637 # re-create windows of data  
638 windows = pysesas.partition(pointcloud, out).getdata()  
639  
640 result = pysesas.spectral(pointcloud[windows[k],:3].astype('float64'))  
641  
642 # get all spectral parameters  
643 result.getdata()  
644  
645 # get the fit parameters for log-log power spectrum  
646 result.getpsdparams()  
647  
648 # get integral lengthscale  
649 result.getlengthscale()  
650  
651 # get spectral moment parameters  
652 result.getmoments()  
653  
654 # get rms and wavelength parameters  
655 result.getlengths()
```

656 Appendix C. Two dimensional tapering

657 A vectorised implementation of a 2D taper is the outer product of two 1D vectors
658 (below denoted A and B) describing window functions of lengths i and j , respectively:

$$T(i, j) = \sqrt{\begin{bmatrix} A_0 \cdot B_0 & A_0 \cdot B_1 & \dots & A_0 \cdot B_j \\ A_1 \cdot B_0 & A_1 \cdot B_1 & \dots & A_1 \cdot B_j \\ \vdots & \vdots & \vdots & \vdots \\ A_i \cdot B_0 & A_i \cdot B_1 & \dots & A_i \cdot B_j \end{bmatrix}}. \quad (17)$$

659 This approach is both highly optimised and allows implementation of any custom
660 (user-defined) 1D window function for tapering. Currently, the `NumPy` taper functions
661 `hanning` (raised cosine), `hamming` (weighted cosine), `bartlett` (triangular) and `blackman`
662 are implemented.

663 Appendix D. Spectral smoothing.

664 The smoothing of power spectral density, $\Psi(\mathbf{K})$ is bin averaged, padded, then con-
665 volved with the Gaussian kernel $g = e^{-2\pi^2\mathbf{K}^2 d\mathbf{K}^2}$ through application of the convolution
666 theorem, such that

$$\mathcal{F}\{\Psi_2(\mathbf{K}) \times g\} = \mathcal{F}\{\Psi_2(\mathbf{K})\} \cdot \mathcal{F}\{g\}, \quad (18)$$

667 where \mathcal{F} denotes Fourier transform. Then the inverse Fourier transform is applied, the
 668 padding removed, and the absolute value taken as the smoothed power spectrum. This
 669 approach takes computational advantage of the fact that smoothing power spectrum with
 670 the kernel then taking derivatives is equivalent to smoothing power spectrum directly
 671 with the derivative of the kernel (Lashermes et al., 2007), or

$$\frac{\delta}{\delta \mathbf{K}} (\Psi_2(\mathbf{K}) \times g) = \Psi_2(\mathbf{K}) \times \frac{\delta g}{\delta \mathbf{K}}. \quad (19)$$

672 Appendix E. Background power spectrum.

673 To summarise briefly, Gaussian random fields are fields drawn from a multivariate
 674 normal distribution that is characterized by its mean and covariance. A Hermitian
 675 random field is drawn from a Gaussian distribution with power spectrum $\Psi(\mathbf{K})$:

$$H(\mathbf{X}_m) = \frac{\mathcal{F}(G(\mathbf{X}_m))}{\sqrt{X_m Y_m}} \sqrt{\Psi_2(\mathbf{K})}, \quad (20)$$

676 where $G(\mathbf{X}_m)$ is a matrix of realisations drawn from a Gaussian ($\mu=0, \sigma=1$) probability
 677 distribution function. The random field is then given as the real part of inverse Fourier
 678 transform of $H(\mathbf{X}_m)$, shifted so the zero-frequency component is at the centre of the
 679 spectrum. The background spectrum is calculated in 2D from the Gaussian field.

680 Appendix F. Spectral slope and intercept.

681 The parameter vector $(\gamma_1, \omega_1)^t$, where t indicates transpose, is calculated as the least-
 682 squares solution of the following over-determined linear system

$$\begin{bmatrix} \log 10[\mathbf{K}_1] & 0 \\ \log 10[\mathbf{K}_2] & 0 \\ \vdots & \vdots \\ \log 10[\mathbf{K}_b] & 0 \end{bmatrix} (\gamma_1, \omega_1)^t = \begin{bmatrix} \log 10[\widehat{\Psi}_{11}] \\ \log 10[\widehat{\Psi}_{12}] \\ \vdots \\ \log 10[\widehat{\Psi}_{1b}] \end{bmatrix}, \quad (21)$$

683 which is solved using the robust linear regression routine provided by the `statsmodels`
 684 module.

685 References

- 686 Aberle, J., Nikora, V., Henning, M., Ettmer, B., Hentschel, B., 2010. Statistical characterization of bed
 687 roughness due to bed forms: A field study in the Elbe River at Aken, Germany. *Water Resources*
 688 *Research* 46, W03521.
- 689 Anderson, J.T., Holliday, D.V., Kloser, R., Reid, D.G., Simard, Y., 2008. Acoustic seabed classification:
 690 current practice and future directions. *ICES Journal of Marine Science* 65, 1004–1011.
- 691 Antonarakis, A.S., Richards, K.S., Brasington, J., 2008. Object-based land cover classification using
 692 airborne LiDAR. *Remote Sensing of the Environment* 112, 2988–2998.
- 693 Antonarakis, A.S., Richards, K.S., Brasington, J., Bithell, M., 2009. Leafless roughness of complex tree
 694 morphology using terrestrial LiDAR. *Water Resources Research* 45, W10401.

- 695 Arnold, N.S., Rees, W.G., Devereux, B.J., Amable, G.S., 2006. Evaluating the potential of high resolution
696 airborne LiDAR data in glaciology. *International Journal of Remote Sensing* 27, 1233–1251. doi:10.
697 1080/01431160500353817.
- 698 Balmino, G., 1993. The spectra of the topography of the Earth, Venus and Mars. *Geophysical Research*
699 *Letters* 20, 1063–1066.
- 700 Beazley, D.M., 2003. SWIG: An extensible compiler for creating scriptable scientific software, in: *Future*
701 *Generation Computer Systems (FGCS) 19*. Elsevier, Amsterdam, pp. 599–609.
- 702 Behnel, S., Bradshaw, R., Citro, C., Dalcin, L., Seljebotn, D.S., Smith, K., 2011. Cython: The best of
703 both worlds. *Computing in Science and Engineering* 13, 31–39. doi:10.1109/MCSE.2010.118.
- 704 Bentley, J.L., 1975. Multidimensional binary search trees used for associative searching. *Communications*
705 *of the ACM* 18, 509–517.
- 706 Berti, M., Corsini, A., Daehne, A., 2013. Comparative analysis of surface roughness algorithms for the
707 identification of active landslides. *Geomorphology* 182, 1 – 18. doi:http://dx.doi.org/10.1016/j.
708 geomorph.2012.10.022.
- 709 Boggs, P.T., Byrd, R.H., Rogers, J.E., Schnabel, R.B., 1992. User's reference guide for ORD-
710 PACK version 2.01 software for weighted orthogonal regression. Technical Report. U.S. Department
711 of Commerce Applied and Computational Mathematics Division. Gaithersburg. URL: http://docs.scipy.org/doc/external/odrpac_guide.pdf.
- 712 Booth, A.M., Roering, J.J., Perron, J.T., 2009. Automated landslide mapping using spectral analysis and
713 high-resolution topographic data: Puget Sound lowlands, Washington, and Portland Hills, Oregon.
714 *Geomorphology* 109, 132–147.
- 715 Brasington, J., Vericat, D., Rychkov, I., 2012. Modeling river bed morphology, roughness, and surface
716 sedimentology using high resolution terrestrial laser scanning. *Water Resources Research* 48, W11519.
- 717 Brodu, N., Lague, D., 2012. 3D terrestrial LiDAR data classification of complex natural scenes using a
718 multi-scale dimensionality criterion: Applications in geomorphology. *ISPRS Journal of Photogram-*
719 *metry and Remote Sensing* 68, 121–134.
- 720 Buckley, S.J., Howell, J.A., Enge, H.D., Kurz, T.H., 2008. Terrestrial laser scanning in geology: data
721 acquisition, processing and accuracy considerations. *Journal of the Geological Society of London* 165,
722 625–638. doi:10.1144/0016-76492007-100.
- 723 Burrough, P., van Gaans, P., MacMillan, R., 2000. High-resolution landform classification using fuzzy
724 k-means. *Fuzzy Sets and Systems* 113, 37–52.
- 725 Buscombe, D., 2013. Transferable wavelet method for grain size-distribution from images of sediment
726 surfaces and thin sections, and other natural granular patterns. *Sedimentology* 60, 1709–1732.
- 727 Buscombe, D., Grams, P.E., Kaplinski, M.A., 2014a. Characterizing riverbed sediments using high-
728 frequency acoustics 1: Spectral properties of scattering. *Journal of Geophysical Research - Earth*
729 *Surface* 119, doi:10.1002/2014JF003189.
- 730 Buscombe, D., Grams, P.E., Kaplinski, M.A., 2014b. Characterizing riverbed sediments using high-
731 frequency acoustics 2: Scattering signatures of Colorado River bed sediments in Marble and Grand
732 Canyons. *Journal of Geophysical Research - Earth Surface* 119, doi:10.1002/2014JF003191.
- 733 Buscombe, D., Rubin, D.M., 2012. Advances in the simulation and automated measurement of well-
734 sorted granular material: 1. Simulation. *Journal of Geophysical Research - Earth Surface* 117, F02001.
- 735 Buscombe, D., Rubin, D.M., Warrick, J.A., 2010. A universal approximation to grain size from images
736 of non-cohesive sediment. *Journal of Geophysical Research - Earth Surface* 115, F02015.
- 737 Campbell, B.A., Garvin, J.B., 1993. Lava flow topographic measurements for radar data interpretation.
738 *Geophysical Research Letters* 20, 831–834. doi:10.1029/93GL00737.
- 739 Carbonneau, P.E., Bergeron, N., Lane, S.N., 2005. Automated grain size measurements from airborne
740 remote sensing for long profile measurements of fluvial grain sizes. *Water Resources Research* 41,
741 W11426. doi:10.1029/2005WR003994.
- 742 Carbonneau, P.E., Lane, S.N., Bergeron, N.E., 2006. Feature based image processing methods applied
743 to bathymetric measurements from airborne remote sensing in fluvial environments. *Earth Surface*
744 *Processes and Landforms* 31, 1413–1423.
- 745 Cartwright, D.E., Longuet-Higgins, M.S., 1956. The statistical distribution of the maxima of a random
746 function. *Proceedings of the Royal Society of London Series A*. 237, 212–232.
- 747 Castelaño, G.P., L. C. Irber, J., Boas, A.V., 2013. An objective reference system for studying rings in the
748 ocean. *Computers and Geosciences* 61, 43–49.
- 749 Cataño-Lopera, Y.A., Abad, J.D., García, M.H., 2009. Characterization of bedform morphology gener-
750 ated under combined flows and currents using wavelet analysis. *Ocean Engineering* 36, 617–632.
- 751 Chan, T.F., Golub, G.H., LeVeque, R.J., 1983. Algorithms for computing the sample variance: Analysis
752 and recommendations. *The American Statistician* 37, 242–247.
- 753

- 754 Church, E.L., 1988. Fractal surface finish. *Applied Optics* 27, 1518–1526.
- 755 Colbo, K., Ross, T., Brown, C., Weber, T., 2014. A review of oceanographic applications of water
756 column data from multibeam echosounders. *Estuarine, Coastal and Shelf Science* 145, 41 – 56.
- 757 Crawford, M., Kumar, S., Ricard, M., Gibeaut, J., Neuenschwander, A., 1999. Fusion of airborne
758 polarimetric and interferometric SAR for classification of coastal environments. *IEEE Transactions*
759 *on Geoscience and Remote Sensing* 37, 1306–1315.
- 760 Dassot, M., Constant, T., Fournier, M., 2011. The use of terrestrial LiDAR technology in forest science:
761 application fields, benefits and challenges. *Annals of Forest Science* 68, 959–974.
- 762 Enßlin, T., Frommert, M., 2011. Reconstruction of signals with unknown spectra in information field
763 theory with parameter uncertainty. *Physical Review D* 83, 105014. doi:10.1103/PhysRevD.83.105014.
- 764 Family, F., 1986. Scaling of rough surfaces: effects of surface diffusion. *Journal of Physics A: Mathe-*
765 *matical and general* 19, L441.
- 766 Fara, H.D., Scheidegger, A.E., 1961. Statistical geometry of porous media. *Journal of Geophysical*
767 *Research* 66, 3279–3284.
- 768 Fonstad, M.A., Dietrich, J.T., Courville, B.C., Jensen, J.L., Carbonneau, P.E., 2013. Topographic
769 structure from motion: a new development in photogrammetric measurement. *Earth Surface Processes*
770 *and Landforms* 38, 421–430.
- 771 Foster, I., 1995. Designing and building parallel programs. doi:ISBN:9780201575941. section 1.4.4.
772 AddisonWesley.
- 773 Fox, C.G., Hayes, D.E., 1985. Quantitative methods for analyzing the roughness of the seafloor. *Reviews*
774 *of Geophysics* 23, 1–48.
- 775 Franceschi, M., Teza, G., Preto, N., Pesci, A., Galgaro, A., Girardi, S., 2009. Discrimination between
776 marls and limestones using intensity data from terrestrial laser scanner. *ISPRS Journal of Photogram-*
777 *metry and Remote Sensing* 64, 522–528.
- 778 Frankel, K.L., Dolan, J.F., 2007. Characterizing arid region alluvial fan surface roughness with airborne
779 laser swath mapping digital topographic data. *Journal of Geophysical Research - Earth Surface* 112,
780 F02025.
- 781 Furbish, D.J., 1987. Conditions for geometric similarity of coarse stream-bed roughness. *Mathematical*
782 *Geology* 19, 291–307.
- 783 Gilman, D.L., Fuglister, F.J., J. M. Mitchell, J., 1963. On the power spectrum of ‘red noise’. *Journal of*
784 *Atmospheric Science* 20, 182–184.
- 785 Glenn, N.F., Streutker, D.R., Chadwick, D.J., Thackray, G.D., Dorsch, S.J., 2006. Analysis of LiDAR-
786 derived topographic information for characterizing and differentiating landslide morphology and ac-
787 tivity. *Geomorphology* 73, 131–148.
- 788 Goff, J.A., Jordan, T.H., 1988. Stochastic modeling of seafloor morphology: Inversion of Sea Beam data
789 for second-order statistics. *Journal of Geophysical Research* B11, 13589–13608.
- 790 Grams, P.E., Topping, D.J., Schmidt, J.C., Hazel, J.E., Kaplinski, M., 2013. Linking morphodynamic
791 response with sediment mass balance on the Colorado River in Marble Canyon: Issues of scale,
792 geomorphic setting, and sampling design. *Journal of Geophysical Research - Earth Surface* 118,
793 361–381.
- 794 Guadagnini, A., Neuman, S.P., 2011. Extended power-law scaling of self-affine signals exhibiting apparent
795 multifractality. *Geophysical Research Letters* 38. doi:10.1029/2011GL047727.
- 796 Hani, A.F.M., Sathyamoorthy, D., Asirvadam, V.S., 2011. A method for computation of surface rough-
797 ness of digital elevation model terrains via multiscale analysis. *Computers and Geosciences* 37, 177 –
798 192. doi:http://dx.doi.org/10.1016/j.cageo.2010.05.021.
- 799 Hildale, R.C., Raff, D., 2008. Assessing the ability of airborne LiDAR to map river bathymetry. *Earth*
800 *Surface Processes and Landforms* 33, 773–783. doi:10.1002/esp.1575.
- 801 Hodge, R., Brasington, J., Richards, K., 2009. In situ characterization of grain-scale fluvial morphology
802 using terrestrial laser scanning. *Earth Surface Processes and Landforms* 34, 954–968.
- 803 Hough, S.E., 1989. On the use of spectral methods for the determination of fractal dimension. *Geophys-*
804 *ical Research Letters* 16, 673–676.
- 805 Huang, J., Turcotte, D.L., 1990. Fractal image analysis: application to the topography of oregon and
806 synthetic images. *Journal of the Optical Society of America A* 7, 1124–1130.
- 807 Huber, P.J., 1981. *Robust Statistics*. John Wiley and Sons, Inc., New York.
- 808 Hunter, J.D., 2007. Matplotlib: A 2D graphics environment. *Computing in Science and Engineering* 9,
809 90–95. doi:10.1109/MCSE.2007.55.
- 810 Jackson, D.R., Richardson, M.D., 2007. *High-frequency seafloor acoustics*. Springer, New York.
- 811 James, M.R., Robson, S., 2012. Straightforward reconstruction of 3D surfaces and topography with a
812 camera: Accuracy and geoscience application. *Journal of Geophysical Research - Earth Surface* 117,

813 F03017. doi:10.1029/2011JF002289.

814 Jerolmack, D.J., Paola, C., 2010. Shredding of environmental signals by sediment transport. *Geophysical*
815 *Research Letters* 37.

816 Jones, E., Oliphant, T., Peterson, P., et al., 2001–. SciPy: Open source scientific tools for Python. URL:
817 <http://www.scipy.org/>. [Online; accessed 2015-02-15].

818 Kalbermatten, M., Ville, D.V.D., Turberg, P., Tuia, D., Joost, S., 2012. Multiscale analysis of geomor-
819 phological and geological features in high resolution digital elevation models using the wavelet trans-
820 form. *Geomorphology* 138, 352 – 363. doi:<http://dx.doi.org/10.1016/j.geomorph.2011.09.023>.

821 Kaplinski, M., Hazel, J.E., Grams, P.E., Davis, P.A., 2014. Monitoring fine-sediment volume in the
822 Colorado River ecosystem, Arizona: Construction and analysis of digital elevation models. U.S.
823 Geological Survey Open-File Report 20141052, 29 p.

824 Kaplinski, M., Hazel, J.E., Parnell, R., Breedlove, M., Kohl, K., Gonzales, M., 2009. Monitoring fine-
825 sediment volume in the Colorado River Ecosystem, Arizona: Bathymetric survey techniques. U.S.
826 Geological Survey Open-file Report 2009–1207, 41 pp.

827 von Karman, T., Howarth, L., 1938. On the statistical theory of isotropic turbulence. *Proceedings of*
828 *the Royal Society London Series A* 164, 192–215.

829 Keller, J.M., Crownover, R.M., Chen, R.Y., 1987. Characteristics of natural scenes related to the fractal
830 dimension. *IEEE Transactions on Pattern Analysis and Machine Intelligence* 9, 621–627.

831 Knuth, D.E., 1998. *The Art of Computer Programming, volume 2: Semi - numerical Algorithms*. 3rd
832 ed., Addison-Wesley, Boston.

833 Krieger, L., Peacock, J.R., 2014. MTPy: A Python toolbox for magnetotellurics. *Computers and*
834 *Geosciences* 72, 167–175.

835 Kukko, A., Anttila, K., Manninen, T., Kaasalainen, S., Kaartinen, H., 2013. Snow surface roughness
836 from mobile laser scanning data. *Cold Regions Science and Technology* 96, 23–35.

837 Lashermes, B., Foufoula-Georgiou, E., Dietrich, W.E., 2007. Channel network extraction from high
838 resolution topography using wavelets. *Geophysical Research Letters* 34, L23S04.

839 Lassueur, T., Joost, S., Randin, C., 2006. Very high resolution digital elevation models: do they improve
840 models of plant species distribution? *Ecological Modelling* 198, 139–153.

841 Legleiter, C.J., Overstreet, B.T., 2012. Mapping gravel-bed river bathymetry from space. *Journal of*
842 *Geophysical Research - Earth Surface* 117, F04024.

843 Longuet-Higgins, M.S., 1975. On the joint distribution of the periods and amplitudes of sea waves.
844 *Journal of Geophysical Research* 80, 2688–2694.

845 Mallet, C., Bretar, F., 2009. Full waveform topographic LiDAR: State-of-the-art. *ISPRS Journal of*
846 *Photogrammetry and Remote Sensing* 64, 1–16.

847 Maneewongvatana, S., Mount, D.M., 1999. It's okay to be skinny, if your friends are fat, in: 4th
848 Annual CGC Workshop on Computational Geometry, Center for Geometric Computing. URL: <http://www.cs.umd.edu/~mount/Papers/cgc99-smpack.pdf>.

849 Manes, C., Guala, M., Löwe, H., Bartlett, S., Egli, L., Lehning, M., 2008. Statistical properties of fresh
850 snow roughness. *Water Resources Research* 44, W11407.

851 Mayer, L.A., 2006. Frontiers in seafloor mapping and visualization. *Marine Geophysical Researches* 27,
852 7–17.

853

854 Mazzarini, F., Pareschi, M.T., Favalli, M., Isola, I., Tarquini, S., Boschi, E., 2007. Lava flow identification
855 and aging by means of LiDAR intensity: Mount Etna case. *Journal of Geophysical Research - Solid*
856 *Earth* 112, B02201.

857 Miller, L., Parsons, C., 1990. Rough surface scattering results based on bandpass autocorrelation forms.
858 *IEEE Transactions on Geoscience and Remote Sensing* 28, 1017–1021.

859 Millman, K.J., Aivazis, M., 2011. Python for scientists and engineers. *Computing in Science and*
860 *Engineering* 13, 9–12. doi:10.1109/MCSE.2011.36.

861 Nelson, P.A., Bellugi, D., Dietrich, W.E., 2014. Delineation of river bed-surface patches by clustering
862 high-resolution spatial grain size data. *Geomorphology* 205, 102–119.

863 Nield, J.M., Wiggs, G.F.S., Squirrell, R.S., 2011. Aeolian sand strip mobility and protodune development
864 on a drying beach: examining surface moisture and surface roughness patterns measured by terrestrial
865 laser scanning. *Earth Surface Processes and Landforms* 36, 513–522.

866 Nikora, V., 2005. High-order structure functions for planet surfaces: A turbulence metaphor. *IEEE*
867 *Geoscience and Remote Sensing Letters* 2, 362–365.

868 Nikora, V.I., Goring, D., Biggs, B.J.F., 1998. On gravel-bed roughness characterisation. *Water Resources*
869 *Research* 34, 517–527.

870 Nitsche, M., Turowski, J.M., Badoux, A., Rickenmann, D., Kohoutek, T.K., Pauli, M., Kirchner, J.W.,
871 2013. Range imaging: a new method for high-resolution topographic measurements in small- and

- 872 medium-scale field sites. *Earth Surface Processes and Landforms* 38, 810–825. doi:10.1002/esp.3322.
- 873 Oliphant, T.E., 2007. Python for scientific computing. *Computing in Science and Engineering* 9, 10–20.
- 874 doi:10.1109/MCSE.2007.58.
- 875 Oppermann, N., Selig, M., Bell, M.R., Enßlin, T.A., 2013. Reconstruction of Gaussian and log-normal
- 876 fields with spectral smoothness. *Physical Review E* 112, 032136.
- 877 Parsons, D.R., Best, J.L., Orfeo, O., Hardy, R.J., Kostaschuk, R., Lane, S.N., 2005. Morphology and
- 878 flow fields of three-dimensional dunes, Rio Parana, Argentina: Results from simultaneous multibeam
- 879 echo sounding and acoustic Doppler current profiling. *Journal of Geophysical Research - Earth Surface*
- 880 110, F04S03.
- 881 Passalacqua, P., Tarolli, P., Foufoula-Georgiou, E., 2010. Testing space-scale methodologies for automatic
- 882 geomorphic feature extraction from LiDAR in a complex mountainous landscape. *Water Resources*
- 883 *Research* 46, W11535.
- 884 Pelgrum, H., Schmutge, T., Rango, A., Ritchie, J., Kustas, B., 2000. Length-scale analysis of surface
- 885 albedo, temperature, and normalized difference vegetation index in desert grassland. *Water Resources*
- 886 *Research* 36, 1757–1765.
- 887 Perron, J.T., Kirchner, J.W., Dietrich, W.E., 2008. Spectral signatures of characteristic spatial scales
- 888 and nonfractal structure in landscapes. *Journal of Geophysical Research - Earth Surface* 113, F04003.
- 889 Pike, R., Wesley, J., 1975. Spectral analysis of landforms. *Annals of the Association of American*
- 890 *Geographers* 65, 499–516.
- 891 Pirotti, F., Tarolli, P., 2010. Suitability of LiDAR point density and derived landform curvature maps
- 892 for channel network extraction. *Hydrological Processes* 24, 1187–1197. doi:10.1002/hyp.7582.
- 893 Pollyea, R.M., Fairley, J.P., 2011. Estimating surface roughness of terrestrial laser scan data using
- 894 orthogonal distance regression. *Geology* 39, 623–626.
- 895 Pollyea, R.M., Fairley, J.P., 2012. Experimental evaluation of terrestrial LiDAR-based surface roughness
- 896 estimates. *Geosphere* 8, 222–228.
- 897 Pradervand, J.N., Dubuis, A., Pellissier, L., Guisan, A., Randin, C., 2014. Very high resolution environ-
- 898 mental predictors in species distribution models: Moving beyond topography? *Progress in Physical*
- 899 *Geography* 38, 79–96. doi:10.1177/0309133313512667.
- 900 Press, W.H., Teukolsky, S.A., Vetterling, W.T., Flannery, B.P., 2007. *Numerical Recipes 3rd Edition:*
- 901 *The Art of Scientific Computing*. Cambridge University Press. doi:ISBN-13:9780521880688.
- 902 Priestley, M.B., 1981. *Spectral analysis and time-series*. Academic Press, New York.
- 903 Ramachandran, P., Varoquaux, G., 2011. Mayavi: 3D Visualization of Scientific Data. *Computing in*
- 904 *Science and Engineering* 13, 40–51.
- 905 Roering, J.J., Mackey, B.H., Marshall, J.A., Sweeney, K.E., Deligne, N.I., Booth, A.M., Handwerker,
- 906 A.L., Cerovski-Darriau, C., 2013. You are HERE: Connecting the dots with airborne LiDAR for
- 907 geomorphic fieldwork. *Geomorphology* 200, 172–183.
- 908 Rothrock, D., Thorndike, A., 1980. Geometric properties of the underside of sea ice. *Journal of Geo-*
- 909 *physical Research: Oceans* 85, 3955–3963.
- 910 Rozema, W., 1968. The use of spectral analysis in describing lunar surface roughness. *U.S. Geological*
- 911 *Survey Professional Paper* 650-D.
- 912 Rushing, J., Ramachandran, R., Nairb, U., Graves, S., Welch, R., Lin, H., 2005. ADaM: A data mining
- 913 toolkit for scientists and engineers. *Computers and Geosciences* 31, 607–618.
- 914 Rychkov, I., Brasington, J., Vericat, D., 2012. Computational and methodological aspects of terrestrial
- 915 surface analysis based on point clouds. *Computers and Geosciences* 42, 64–70.
- 916 Sankey, J.B., Glenn, N.F., Germino, M.J., Gironella, A.I.N., Thackray, G.D., 2010. Relationships of
- 917 aeolian erosion and deposition with LiDAR-derived landscape surface roughness following wildfire.
- 918 *Geomorphology* 119, 135–145.
- 919 Savitzky, A., Golay, M.J.E., 1964. Smoothing and differentiation of data by simplified least squares
- 920 procedures. *Analytical Chemistry* 36, 1627–1639.
- 921 Sayles, R.S., Thomas, T.R., 1978. Surface topography as a nonstationary random process. *Nature* 271,
- 922 431–434.
- 923 Selig, M., Bell, M.R., Junklewitz, H., Oppermann, N., Reinecke, M., Greiner, M., Pachajoa, C., Enßlin,
- 924 T.A., 2013. NIFTY - Numerical information field theory - a versatile Python library for signal
- 925 inference. *Astronomy and Astrophysics* 554, A26.
- 926 Shepard, M.K., Brackett, R.A., Arvidson, R.E., 1995. Self-affine (fractal) topography: Surface pa-
- 927 rameterization and radar scattering. *Journal of Geophysical Research: Planets* 100, 11709–11718.
- 928 doi:10.1029/95JE00664.
- 929 Shepard, M.K., Campbell, B.A., Bulmer, M.H., Farr, T.G., Gaddis, L.R., Plaut, J.J., 2001. The rough-
- 930 ness of natural terrain: A planetary and remote sensing perspective. *Journal of Geophysical Research:*

931 Planets 106, 32777–32795. doi:10.1029/2000JE001429.

932 Singh, A., Fofoula-Georgiou, E., Port-Agel, F., Wilcock, P.R., 2012. Coupled dynamics of the co-
933 evolution of gravel bed topography, flow turbulence and sediment transport in an experimental chan-
934 nel. *Journal of Geophysical Research - Earth Surface* 117, F04016.

935 Smith, M.W., 2014. Roughness in the Earth Sciences. *Earth-Science Reviews* 136, 202–225.

936 Tarolli, P., 2014. High-resolution topography for understanding Earth surface processes: Opportunities
937 and challenges. *Geomorphology* 216, 295–312.

938 Taylor, G.I., 1938. The spectrum of turbulence. *Proceedings of the Royal Society London Series A* 164,
939 476–490.

940 Trevisani, S., Cavalli, M., Marchi, L., 2012. Surface texture analysis of a high-resolution DTM: Interpret-
941 ing an alpine basin. *Geomorphology* 161162, 26 – 39. doi:[http://dx.doi.org/10.1016/j.geomorph.](http://dx.doi.org/10.1016/j.geomorph.2012.03.031)
942 [2012.03.031](http://dx.doi.org/10.1016/j.geomorph.2012.03.031).

943 Turcotte, D., 1992. *Fractals and Chaos in Geology and Geophysics*. Cambridge Univ. Press, Cambridge.

944 Vierling, K.T., Vierling, L.A., Gould, W.A., Martinuzzi, S., Clawges, R.M., 2008. LiDAR: shedding new
945 light on habitat characterization and modeling. *Frontiers in Ecology and the Environment* 6, 90–98.

946 van der Walt, S., Colbert, S.C., Varoquaux, G., 2011. The NumPy array: A structure for efficient
947 numerical computation. *Computing in Science and Engineering* 13, 22–30. doi:10.1109/MCSE.2011.37.

948 Warrick, J.A., Rubin, D.M., Ruggiero, P., Harney, J., Draut, A.E., Buscombe, D., 2009. Cobble cam:
949 grain-size measurements of sand to boulder from digital photographs and autocorrelation analyses.
950 *Earth Surface Processes and Landforms* 34, 1811–1821.

951 Welford, B.P., 1962. Note on a method for calculating corrected sums of squares and products. *Techno-*
952 *metrics* 4, 419–420.

953 Wellmann, J.F., Croucher, A., Regenauer-Lieb, K., 2012. Python scripting libraries for subsurface fluid
954 and heat flow simulations with TOUGH2 and SHEMAT. *Computers and Geosciences* 43, 197–206.

955 Westoby, M., Brasington, J., Glasser, N., Hambrey, M., Reynolds, J., 2012. Structure-from-motion
956 photogrammetry: A low-cost, effective tool for geoscience applications. *Geomorphology* 179, 300–314.

957 Wheaton, J.M., Brasington, J., Darby, S.E., Merz, J., Pasternack, G.B., Sear, D., Vericat, D., 2010.
958 Linking geomorphic changes to salmonid habitat at a scale relevant to fish. *River Research and*
959 *Applications* 26, 469–486. doi:10.1002/rra.1305.

960 Whitehouse, D., 1997. Surface metrology. *Measurement Science and Technology* 8, 955–972.

961 Wieland, R., Dalchow, C., 2009. Detecting landscape forms using Fourier transformation and singular
962 value decomposition(SVD). *Computers and Geosciences* 35, 1409–1414.

963 Wilson, T.H., Dominic, J., 1998. Fractal inter-relationships between topography and structure. *Earth*
964 *Surface Processes and Landforms* 23, 509–525.

965 Woodget, A., Carbonneau, P., Visser, F., Maddock, I., 2015. Quantifying submerged fluvial topography
966 using hyperspatial resolution uas imagery and structure from motion photogrammetry. *Earth Surface*
967 *Processes and Landforms* 40, 47–64.

968 Wright, S.A., Kaplinski, M., 2011. Flow structures and sandbar dynamics in a canyon river during
969 a controlled flood, Colorado River, Arizona. *Journal of Geophysical Research - Earth Surface* 116,
970 F01019.

971 van Zyl, J., Burnette, C., Farr, T., 1991. Inference of surface power spectra from inversion of multifre-
972 quency polarimetric radar data. *Geophysical Research Letters* 18, 1787–1790.

973 **Table captions**

- 974 (1) PySESA sub-modules (to date) and their functions.

975 **Figure captions**

- 976 (1) A schematic of a basic PySESA workflow (read left to right) and the sub-modules
977 responsible for carrying out tasks.
- 978 (2) Illustration of the data windowing procedure controlled by the `PySESA::partition`
979 parameter ‘percent overlap’. A dense point cloud is analysed such that is decimated
980 to a regular $1\text{m} \times 1\text{m}$ grid (red dots) by using increasing amounts of data: a) -50%
981 overlap; b) 0% overlap (program default); c) 50% overlap; and d) 100% overlap.
- 982 (3) Each of the 4 subplots shows the same point cloud (red dots) in a small area typical
983 of a window of data, and the 2D function fit through that point cloud (blue surface)
984 for the purposes of detrending. The 4 detrending methods currently implemented in
985 PySESA are a) Ordinary Least Squares (OLR); b) Robust Linear Regression (RLR);
986 c) Orthogonal Distance Regression (ODR); and d) Savitsky-Golay digital filter of
987 any order (shown is order 0). The detrending effects on the point cloud are shown
988 by the standard deviation of detrended amplitudes, denoted σ in each subplot, and
989 which range from 6.1cm (ODR) to 29.1cm (RLR).
- 990 (4) The distribution of residuals created by detrending the point clouds in the corre-
991 sponding 4 subplots of Figure 3.
- 992 (5) a) The raw point cloud used to demonstrate the functionality of the PySESA toolbox.
993 This is a bathymetric point cloud, obtained using multibeam echosounder, of a 60
994 $\times 80\text{m}$ patch of the Colorado River bed in Western Grand Canyon, around river
995 mile 224. The point cloud, composed of almost 1 million 3D points, clearly shows
996 areas of varying textures, including sand dunes, flat sand areas, and rocky areas. b)
997 A different perspective on the same scene, to better show the variation in heights
998 across the data.
- 999 (6) The point cloud shown in Figure 5a, decimated to a $0.25 \times 0.25\text{m}$ regular grid by
1000 the PySESA program, and colour-coded by: a) spectral root-mean-square variation
1001 in amplitude, σ (m); and b) spectral strength ω_2 (m^4).
- 1002 (7) Contour maps of gridded (0.25×0.25 m) parameters from spatial and spectral
1003 analyses of the point cloud shown in Figure 5. In each subplot, just a small $70 \times 45\text{m}$
1004 portion of the data is shown. The parameters shown are: a) elevation; b) spectral
1005 strength; c) spectral slope; d) integral lengthscale; e) spectral width; f) standard
1006 deviation; g) detrended standard deviation; h) spectral standard deviation; i) ratio
1007 of integral lengthscale and standard deviation; and j) skewness.
- 1008 (8) Processing times for increasing numbers of 3D points in the point cloud, for process-
1009 ing for a a) 4-core Intel[®] Xeon[®] W3530 CPU at 2.80GHz; and a b) 8-core Intel[®]
1010 Core[®] i7-3630QM CPU at 2.40GHz. The overall differences in the processing times
1011 show how distributing the computation over more CPUs (b) is more beneficial than
1012 a faster CPU (a). Different symbols refer to the degree of overlap in the windowing
1013 procedure. Connected symbols show processing times all spatial parameters using
1014 `PySESA::spatial` and unconnected symbols show processing times all spatial and
1015 spectral parameters using `PySESA::spectral`.

1016 (9) The percentage speedup associated with processing with an 8-core 2.40 GHz com-
1017 pared with a 4-core 2.80GHz processor, for a) all spatial and spectral parameters us-
1018 ing `PySESA::spectral`, and b) processing all spatial parameters using `PySESA::spatial`.
1019 Different symbols refer to the degree of overlap in the windowing procedure.

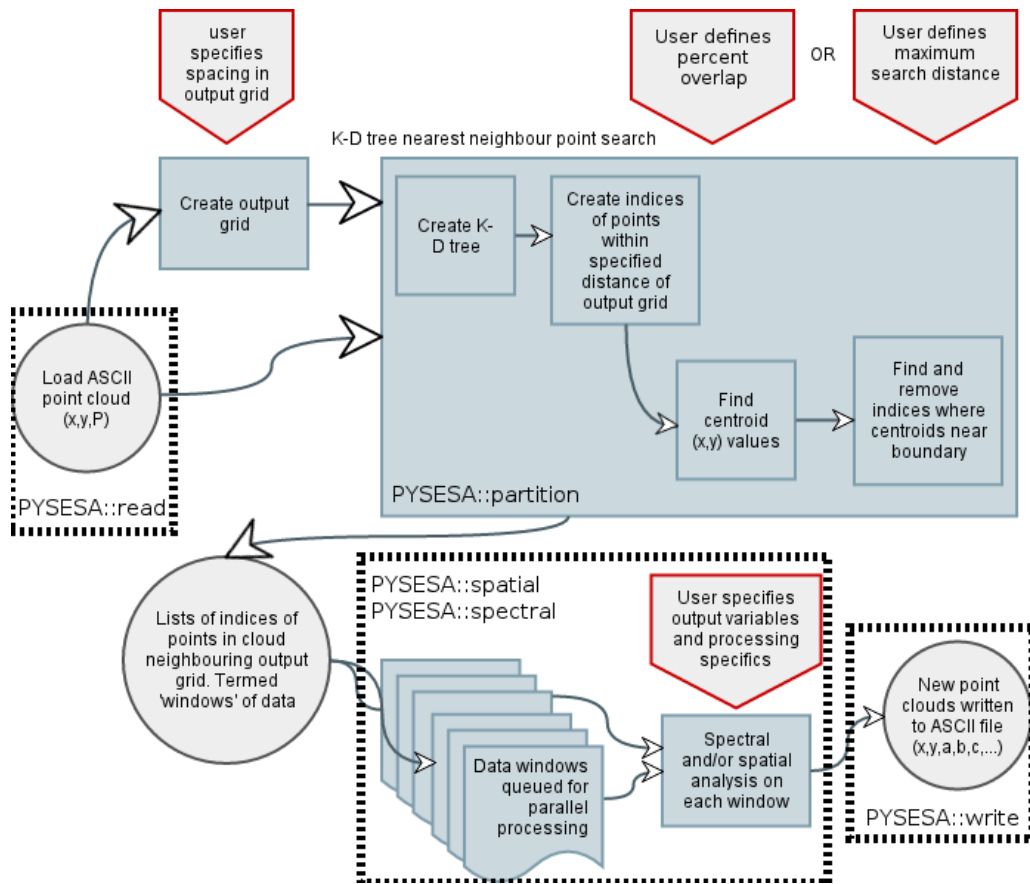


Figure 1: A schematic of a basic PySESA workflow (read left to right) and the sub-modules responsible for carrying out tasks.

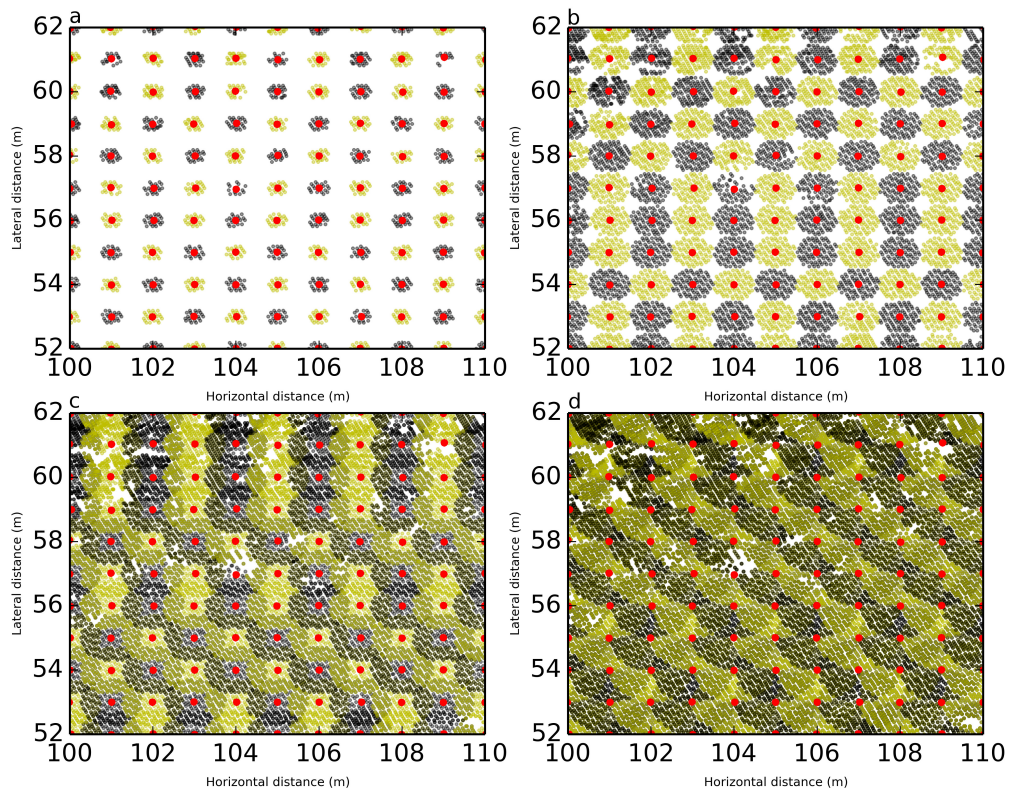


Figure 2: Illustration of the data windowing procedure controlled by the `PySESA::partition` parameter 'percent overlap'. A dense point cloud is analysed such that is decimated to a regular $1\text{m} \times 1\text{m}$ grid (red dots) by using increasing amounts of data: a) -50% overlap; b) 0% overlap (program default); c) 50% overlap; and d) 100% overlap.

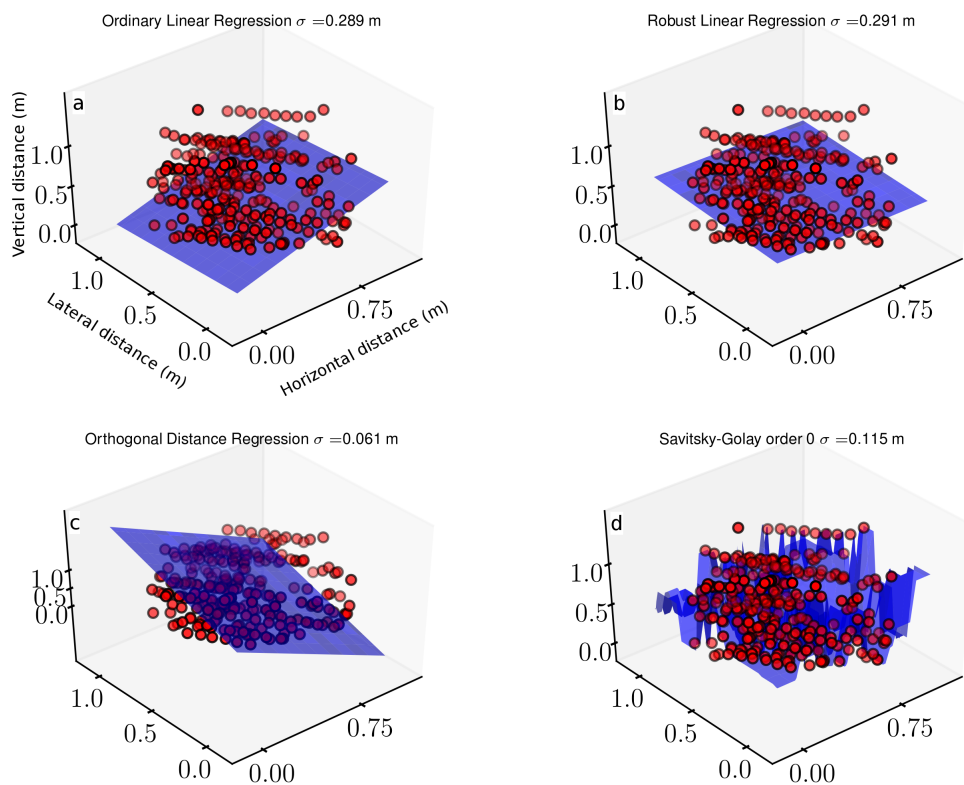


Figure 3: Each of the 4 subplots shows the same point cloud (red dots) in a small area typical of a window of data, and the 2D function fit through that point cloud (blue surface) for the purposes of detrending. The chosen point cloud shows a high degree of clustering in space, which means that the 4 detrending methods currently implemented in PySESA give very different trends through the data. These method choices are a) Ordinary Least Squares (OLR); b) Robust Linear Regression (RLR); c) Orthogonal Distance Regression (ODR); and d) Savitsky-Golay digital filter of any order (shown is order 0). The detrending effects on the point cloud are shown by the standard deviation of detrended amplitudes, denoted σ in each subplot, and which range from 6.1cm (ODR) to 29.1cm (RLR).

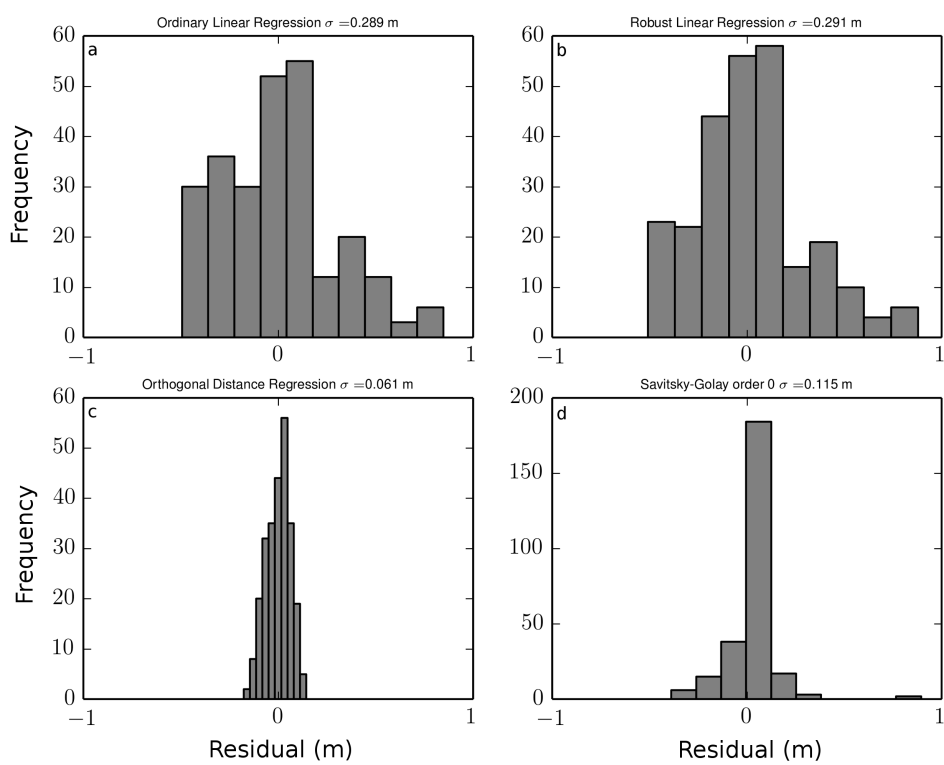


Figure 4: The distribution of residuals created by detrending the point clouds in the corresponding 4 subplots of Figure 3.

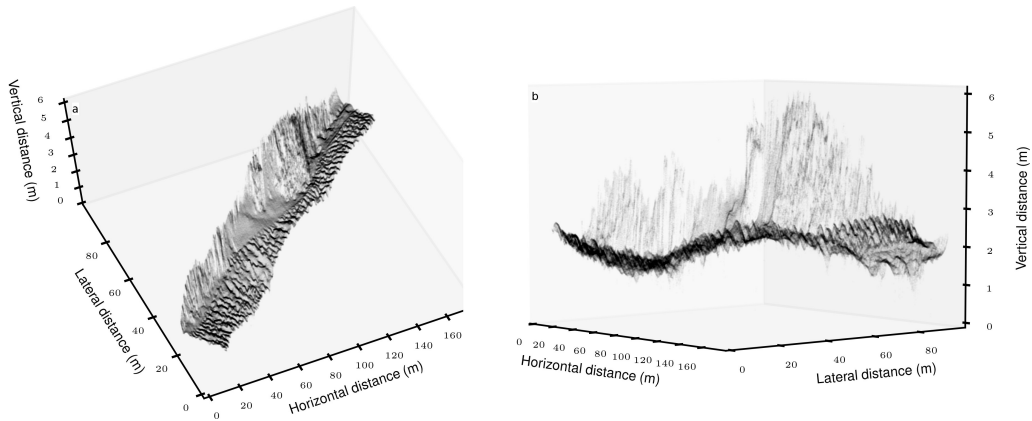


Figure 5: a) The raw point cloud used to demonstrate the functionality of the PySESA toolbox. This is a bathymetric point cloud, obtained using multibeam echosounder, of a $60 \times 80\text{m}$ patch of the Colorado River bed in Western Grand Canyon, around river mile 224. The point cloud, composed of almost 1 million 3D points, clearly shows areas of varying textures, including sand dunes, flat sand areas, and rocky areas. b) A different perspective on the same scene, to better show the variation in heights across the data.

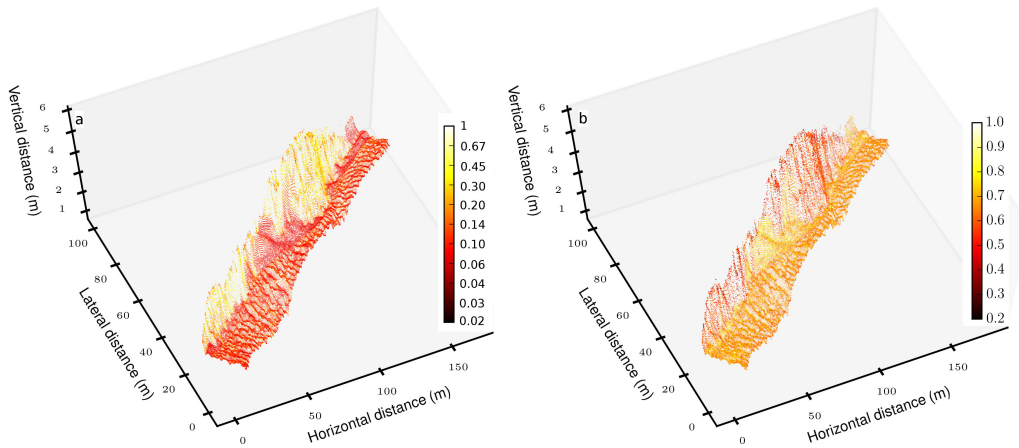


Figure 6: The point cloud shown in Figure 5a, decimated to a $0.25 \times 0.25\text{m}$ regular grid by the PySESA program, and colour-coded by: a) spectral root-mean-square variation in amplitude, σ (m); and b) spectral strength ω_2 (m^4).

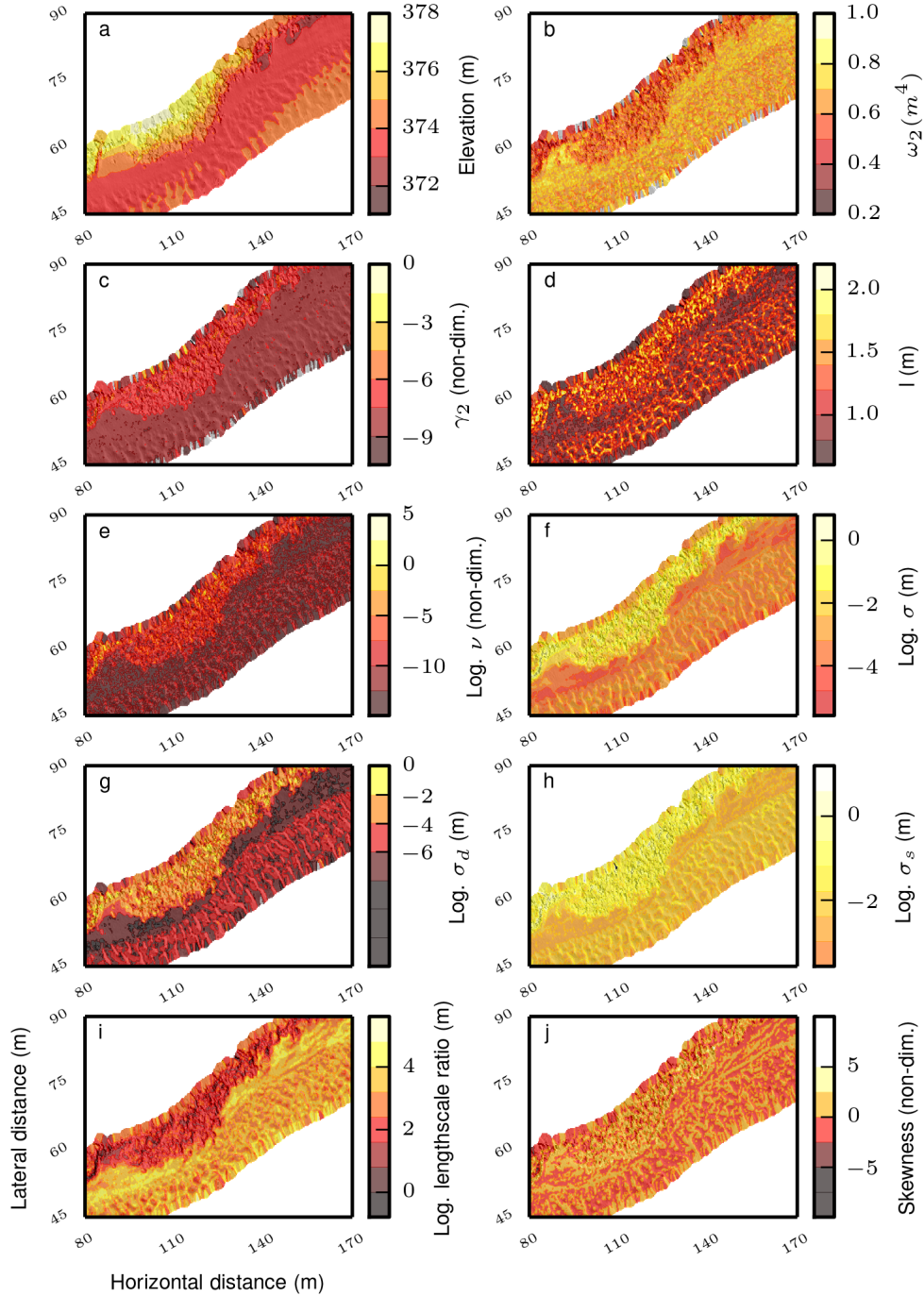


Figure 7: Contour maps of gridded (0.25×0.25 m) parameters from spatial and spectral analyses of the point cloud shown in Figure 5. In each subplot, just a small 70×45 m portion of the data is shown. The parameters shown are: a) elevation; b) spectral strength; c) spectral slope; d) integral lengthscale; e) spectral width; f) standard deviation; g) detrended standard deviation; h) spectral standard deviation; i) ratio of integral lengthscale and standard deviation; and j) skewness.

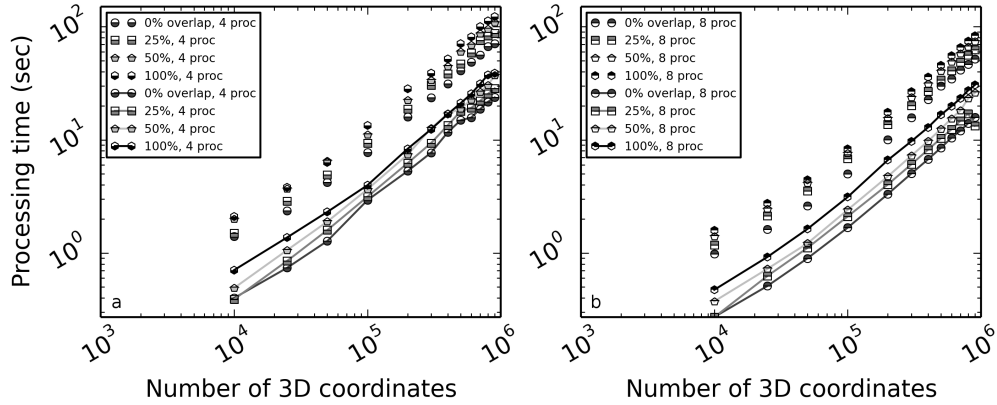


Figure 8: Processing times for increasing numbers of 3D points in the point cloud, for processing for a) a 4-core Intel[®] Xeon[®] W3530 CPU at 2.80GHz; and a b) 8-core Intel[®] Core[®] i7-3630QM CPU at 2.40GHz. The overall differences in the processing times show how distributing the computation over more CPUs (b) is more beneficial than a faster CPU (a). Different symbols refer to the degree of overlap in the windowing procedure. Connected symbols show processing times all spatial parameters using `PySESA::spatial` and unconnected symbols show processing times all spatial and spectral parameters using `PySESA::spectral`.

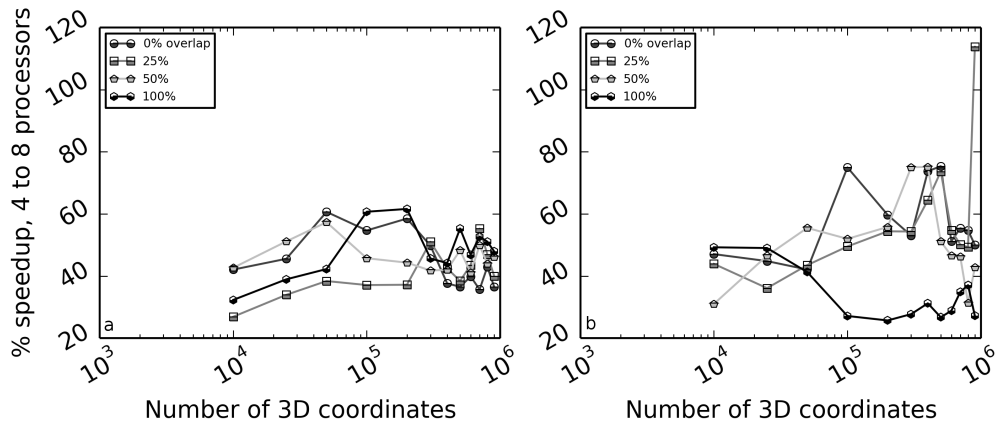


Figure 9: The percentage speedup associated with processing with an 8-core 2.40 GHz compared with a 4-core 2.80GHz processor, for a) all spatial and spectral parameters using `PySESA::spectral`, and b) processing all spatial parameters using `PySESA::spatial`. Different symbols refer to the degree of overlap in the windowing procedure.

Table 1: PySESA sub-modules (to date) and their functions.

PySESA sub-module	Function
read	read a 3-column space, comma or tab delimited text file
partition	partition a $N \times 3$ point cloud ($P = [X, Y, Z]$) into m windows of $n \times 3$ points (\mathbb{P}_m) with specified spacing between centroids of adjacent windows and with specified overlap between windows.
detrend	<code>.getdata()</code> returns detrended amplitudes of a $N \times 3$ point cloud
sgolay	<code>.getdata()</code> returns the Savitsky-Golay digital filter of a 2D signal
spatial	calculate spatial statistics of a $N \times 3$ point cloud <code>.getdata()</code> returns: x = centroid in horizontal coordinate y = centroid in lateral coordinate z_mean = centroid in amplitude z_max = max amplitude z_min = min amplitude z_range = range in amplitude sigma (σ or σ_d , unit amplitude) = standard deviation of amplitudes skewness (non-dim.) = skewness of amplitudes kurtosis (non-dim.) = skewness of amplitudes n = number of 3D coordinates
RunningStats	called by spatial to compute sigma, skewness and kurtosis
lengthscale	calculates the integral lengthscale of a $N \times 3$ point cloud
spectral	calculate spectral statistics of a $N \times 3$ point cloud <code>.getdata()</code> returns: slope (γ_1 , non-dim.) = slope of regression line through log-log 1D power spectral density (PSD) intercept (ω_1 , unit length ⁴) = intercept of regression line through log-log 1D PSD r_value (non-dim.) = correlation of regression through log-log 1D PSD p_value (non-dim.) = probability that slope of regression through log-log 1D PSD is not zero std_err (unit amplitude) = standard error of regression through log-log 1D PSD d (D , non-dim.) = fractal dimension l (l_0 , unit length) = integral lengthscale wmax (λ_{max} , unit length) = peak wavelength wmean (λ_{mean} , unit length) = mean wavelength rms1 (σ_1 , unit amplitude) = root-mean-square (RMS) amplitude from PSD rms2 (σ_1 , unit amplitude) = RMS amplitude from bin averaged PSD Z (N_0) = zero-crossings per unit length E (E_0) = extreme per unit length sigma (σ_m , unit amplitude) = RMS amplitude from spectral moments T0.1 (λ , unit length) = average spatial period (m_0/m_1) T0.2 (λ , unit length) = average spatial period (m_0/m_2) ^{0.5} sw1 (ν , non-dim.) = spectral width sw2 (ν , non-dim.) = spectral width (normalised radius of gyration) m0 (m_0) = zeroth moment of spectrum m1 (m_1) = first moment of spectrum m2 (m_2) = second moment of spectrum m3 (m_3) = third moment of spectrum m4 (m_4) = fourth moment of spectrum phi (ϕ , degrees) = effective slope
process	allows control of inputs to all modules (full workflow)
write	write program outputs to a comma delimited text file
plot	various utilities for plotting raw and decimated point clouds and grids in 2D and 3D
test	program testing suite